



1 **Estimating surface mass balance patterns from UAV measurements**
2 **on the ablation area of the Morteratsch-Pers glacier complex**
3 **(Switzerland)**
4

5 Lander VAN TRICHT^{1,*}, Philippe HUYBRECHTS¹, Jonas VAN BREEDAM¹, Alexander
6 VANHULLE¹, Kristof VAN OOST², Harry ZEKOLLARI³
7

8 ¹Earth System Science & Departement Geografie, Vrije Universiteit Brussel, Brussels, Belgium

9 ²Georges Lemaître Center for Earth & Climate Research, Earth and Life Institute, Université catholique de
10 Louvain, Louvain-la-Neuve, Belgium

11 ³Department of Geoscience and Remote Sensing, Delft University of Technology, Delft, Netherlands
12

13 **Corresponding author: Lander Van Tricht (lander.van.tricht@vub.be)*
14

15 **Abstract.** The surface mass balance of a glacier (SMB) provides the link between the glacier and the local climate.
16 For this reason, it is intensively studied and monitored. However, major efforts are required to determine the SMB
17 on a sufficient number of locations to capture the heterogeneity of the SMB pattern. Furthermore, because of the
18 time-consuming and costly nature of these measurements, detailed SMB measurements are carried out on only a
19 limited number of glaciers. In this study, we investigate how to accurately determine the SMB in the ablation zone
20 of Vadret da Morteratsch and Vadret Pers (Engadin, Switzerland) using the continuity-equation method. For this,
21 an elaborate dataset (spanning the 2017-2020 period) of high-resolution data derived from UAV measurements
22 (surface elevation changes and surface velocities) is combined with reconstructed ice thickness fields (based on
23 radar measurements). To determine the performance of the method, we compare modelled SMB with measured
24 SMB values at the position of stakes. Our results indicate that with annual UAV surveys, it is possible to obtain
25 SMB estimates with a mean absolute error of approximately 0.5 metre ice equivalent per year. Yet, our study
26 demonstrates that in order to obtain these accuracies, it is necessary to consider the ice flow over spatial scales of
27 several times the local ice thickness using an exponential decay filter. Furthermore, our study shows the crucial
28 importance of the ice thickness, which must be sufficiently well known in order to apply the method. The latter
29 currently hampers the application of the continuity-equation method to derive detailed SMB patterns on regional
30 to global scales.
31
32



33 **1 Introduction**

34

35 The surface mass balance of a glacier is determined by the processes adding mass to the surface (e.g. snow fall,
36 freezing rain), and those removing mass from the surface (e.g. snow and ice melt, sublimation). These processes
37 are strongly driven by the local temperature and precipitation over the glacier. As a result of increased global mean
38 temperatures, SMBs are becoming increasingly negative, leading to an unprecedented shrinkage of glaciers during
39 the last decade (Zemp et al., 2019; Wouters et al., 2019). Because of the direct link with the local climatic signal,
40 determining the glacier surface mass balance and its distribution is crucial to monitor, understand and model the
41 reaction of glaciers to climate change. Traditionally, a stake and snow pit network is used to determine the SMB
42 at a small number of positions followed by an inter- and extrapolation to obtain the glacier average specific mass
43 balance (Braithwaite, 2002). This can result in large errors for glaciers where the heterogeneity of the SMB cannot
44 be captured sufficiently by the available measurements (Zemp et al., 2013). Further, because of the time-
45 consuming and costly nature of these measurements, detailed SMB measurements are carried out on only a limited
46 number of glaciers.

47

48 Geodetic methods provide an alternative, and have lately been applied in numerous studies, to monitor mass
49 balances for individual glaciers at local to regional scales (e.g. Brun et al., 2017; Davaze et al., 2020; Sommer et
50 al., 2020). These methods all involve comparing digital elevation models (DEMs), mainly created using airborne
51 and satellite data, over a given period to determine local elevation changes. These local elevation changes result
52 from an interaction between mass balance and ice flow processes and do therefore not allow to directly determine
53 the mass balance distribution over glaciers. However, having such a mass balance distribution over glaciers is of
54 large interest, as this can be used to accurately calibrate mass balance models used in large-scale glacier modelling
55 efforts to allow for example for an accurate calibration of mass balance gradients (Zekollari et al., 2018; Marzeion
56 et al., 2020).

57

58 Several studies have attempted to determine patterns of SMB from surface elevation changes by implementing
59 either mass-continuity, a kinematic boundary condition at the surface or through 3D ice flow modelling (Kääb and
60 Funk, 1999; Gudmundsson and Bauder, 1999; Hubbard et al., 2000; Reeh et al., 2002; Nuimura et al., 2011;
61 Vincent et al., 2016; Bisset et al., 2020). In essence, these are all based on the principle of combining surface
62 elevation changes with the ice flux divergence. While the former can be measured directly, the latter is calculated
63 by combining various types of measurements. Most of previous studies stumbled on the necessity, resulting from
64 the discretization of ice flow processes and spatial resolution of the data, to smooth the input data or the ice flux
65 divergence or to resample to much lower resolutions of several hundreds of metres. Further, a recurring drawback
66 in previous studies attempting to detect local and small-scale variations of the SMB was the lack of satellite
67 observations with sufficient spatial and temporal resolution (Ryan et al., 2015). However, with the emergence of
68 Unmanned Aerial Vehicles (UAV), it turned out to be possible to detect small scale variations at unprecedented
69 centimetre resolution. In recent years, studies have attempted to determine the SMB at the location of individual
70 ablation stakes using an UAV and with measured vertical velocities (e.g. Vincent et al., 2020). However, to our
71 knowledge, no research has yet been carried out to derive a transferable method to determine the SMB distribution
72 over an entire ablation zone using multiannual UAV measurements. Furthermore, the optimal ways to calculate



73 the ice flux divergence, and how to represent the spatial scales over which ice flow occurs without resampling to
74 a much lower resolution, remain a topic of discussion.

75

76 The aim of this study consists of deriving and applying a method to determine the SMB in the entire ablation zone
77 of two glaciers by combining UAV acquired 3D data and ice thickness measurements through the continuity-
78 equation method. We pay particular attention to the spatial scales that need to be considered in this framework and
79 how these influence the modelled SMB. The performance is evaluated through an in-depth comparison with
80 measured SMB at stakes. To allow the method to be applied for other glaciers, with different data availability, we
81 also perform a comprehensive sensitivity analysis, from which we determine which data is crucial in the
82 application of the method and its accuracy.

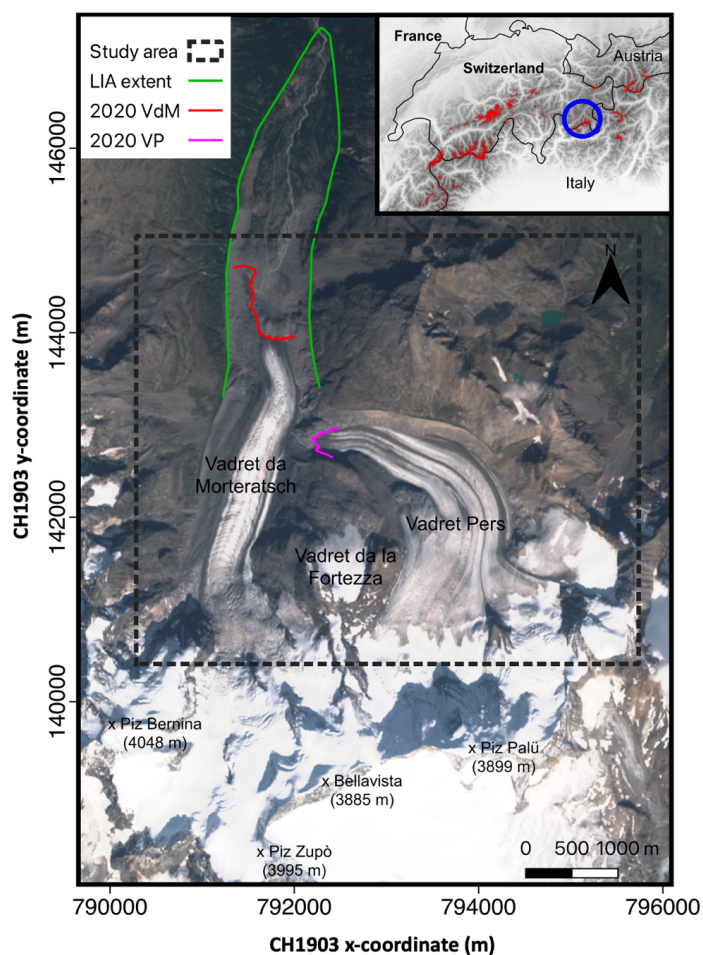
83

84

85 **2 Study area and fieldwork**

86

87 The current study focuses on the Morteratsch - Pers glacier complex situated in the Bernina massif in the
88 southeastern part of Switzerland (European Alps) (Figure 1). Vadret da Morteratsch, with a current length of
89 approximately 6 km, is the main glacier and flows from the south to the north. Vadret Pers, which flows towards
90 Vadret da Morteratsch from the southeast, became a separate glacier in 2015, when both glaciers disconnected
91 (Zekollari and Huybrechts, 2018). At present, the two glaciers cover an area of about 15 km² with a volume of ca.
92 1 km³ making it the largest continuous ice area in the Bernina region. Vadret da Morteratsch reached its maximum
93 Little Ice Age (LIA) extent between 1860 and 1865 (Zekollari et al., 2014). Since 1878, the glacier front has
94 retreated more than three kilometres and is nowadays located at an altitude of 2200 m above sea level (a.s.l). The
95 upper parts of the glacier complex reach 4000 m a.s.l, originating at peaks such as Piz Bernina and Bellavista
96 (Figure 1). The glacier complex has been studied and monitored intensively with SMB stake measurements
97 performed annually at the end of the ablation season since 2001 (Zekollari and Huybrechts, 2018). In addition, the
98 geodetic mass balance of the 1980-2010 period was determined to be between -0.7 and -0.8 metre water equivalent
99 per year (Fischer et al., 2015). The SMB stake measurements served to calibrate a mass balance model (Nemec et
100 al., 2009) which was coupled to a higher-order ice flow model to simulate the future evolution of the glacier
101 complex (Zekollari et al., 2014) and to study its response time (Zekollari and Huybrechts, 2015). Furthermore, the
102 ice thickness in the ablation area has been measured twice (Zekollari et al., 2013; Langhammer et al., 2019) and
103 again in 2020 for specific parts of Vadret da Morteratsch.



104

105

106 **Figure 1.** Map of the Morteratsch-Pers glacier complex in southeastern Switzerland. The different coloured lines represent
107 the extent of the glacier at the end of the Little Ice Age (LIA, 1860-1865) and in 2020. The background image is a Sentinel-2
108 true colour composite satellite image from 13 September 2020. The highest mountains are labelled and indicated with a black
109 cross. The inset shows a DEM of the Shuttle Radar Topography Mission (SRTM) and boundaries of the countries of the central
110 and western European Alps. The areas indicated with a red colour are glaciers according to the Randolph Glacier Inventory
111 (RGI) version 6. The location of the Morteratsch-Pers glacier complex is indicated with a blue circle.

112

113

114 2.1 UAV surveys

115

116 Between 2017 and 2020, we conducted annual UAV surveys at the end of the ablation season (late September).
117 Hence, the focus in this research is on three mass-balance years (2017-2018, 2018-2019 and 2019-2020). In 2017,
118 above normal snow cover prevented drone mapping on the upper parts of the ablation area of Vadret Pers (>2800



119 m) due to inadequate visual content for accurate keypoint detection (Gindraux et al., 2017). This resulted in a
120 smaller study area in 2017-2018. The observations consist of images acquired by repeated UAV surveys with a
121 DJI Phantom 4 Pro (P4PRO) (in 2017, 2018 and 2019) and a DJI Phantom 4 RTK (P4RTK) (in 2020) quadcopter,
122 both equipped with a 20-megapixel camera. For flight planning and UAV piloting, DJI GS Pro was used. The
123 flight plans were designed to limit the variation in ground sampling distance (GSD) by flying parallel to the main
124 surface slope and by subdividing the study area into smaller sections. Additional technical details of the flights are
125 given in Table 1. The different flights within one field campaign were performed on multiple days. However,
126 because of the limited surface change during the fieldwork periods (4-6 days), no correction was applied for the
127 difference in acquisition dates.

128

129

130 *Table 1. Technical details of the UAV flights.*

131

Setting	Value
Flight altitude	On average 180 m
Ground resolution	5-10 cm
View angle	90°
Flight speed	5 m/s
Capture interval	4 s
Frontal overlap	90%
Side overlap	70%

132

133

134 To ensure sufficient horizontal and vertical accuracy, ground control points (GCPs) were distributed over the area
135 of interest. The GCPs, plastic orange squares of 40x40 cm, were measured with a Trimble 7 GeoXH RTK GPS
136 (horizontal average accuracy of 10-20 cm, vertical average accuracy of 20-30 cm) by relying on the swipos
137 positioning service. The GCPs were spread over different locations on the glacier following density and
138 distribution guidelines from the literature (Tahar et al., 2012; Goldstein et al., 2015; Long et al., 2016; Tonkin et
139 al., 2016; Gindraux et al., 2017). We ensured homogeneous distribution in almost every case, except where
140 crevasses, moulins or a fresh layer of snow (especially in 2017) impeded this with an average density of 10-20
141 GCPs km⁻². In 2020, a smaller number of GCPs was placed because the P4RTK can achieve centimetre-level
142 accuracy without a large number of GCPs as a result of an on-board differential GPS system (Zhang et al., 2019;
143 Kienholz et al., 2020).

144

145

146 **2.2 In situ surface mass balance data**

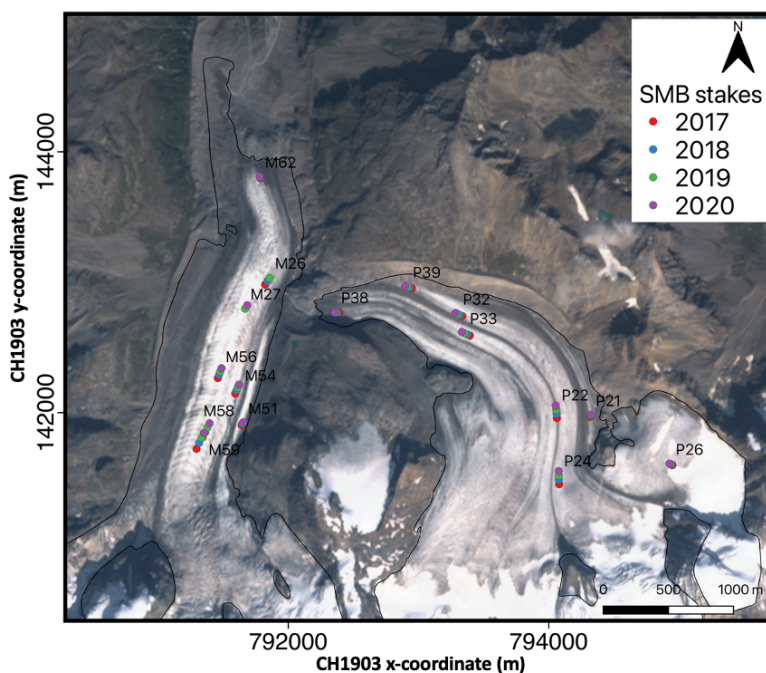
147

148 A total of 287 annual mass balance stake measurements (158 on Morteratsch, 129 on Pers) were performed
149 between 2001 and 2020 in the ablation area of the glacier complex. All the stakes were located between 2100 and
150 2600 m a.s.l. on the Morteratsch glacier's ablation tongue and between 2450 and 3050 (approximately the ELA)
151 on Vadret Pers. Zekollari and Huybrechts (2018) summarized these measurements and found the SMB on Pers
152 glacier to be significantly lower (2.1-2.5 metres ice equivalent (m i.e.) yr⁻¹) compared to Vadret da Morteratsch at



153 similar elevation. This has been mainly attributed to differences in orientation and the associated daily insolation
154 cycle over the two glaciers. For the period of concern in this study (2017-2020), SMB measurements from 16
155 individual stakes (8 on each glacier) are available for every year on the debris-free part of the ablation areas (Figure
156 2). The stakes were measured, and replaced if necessary, annually at the end of each ablation season, during the
157 UAV surveys.

158
159



160

161

162 **Figure 2.** Satellite image of the study area with the location of the measured ablation stakes in 2017, 2018, 2019 and 2020.
163 The background image is a Sentinel-2 true colour composite satellite image from 13 September 2020. The different locations
164 of the stakes in 2017-2018-2019-2020 show the movement of the stakes with the glacier flow. The labels refer to the stake
165 names as used in the fieldwork programme. In 2019, stake M26, which was located in the middle of a crevasse field, was
166 replaced by stake M27.

167

168

169 2.3 Ice thickness data

170

171 To calculate the local ice volume flux divergence (see section 3.4), a distribution of the ice thickness is required.
172 There are two published datasets of the ice thickness of the Morteratsch – Pers glacier complex, derived from radar
173 measurements (especially in the ablation area) and modelling (especially in the accumulation area). The first one
174 is the dataset of Zekollari et al. (2013), hereafter referred to as THIZ. This distribution was reconstructed by
175 combining measured ice thicknesses (~30 ground borne GPR profiles in the early 2000s) with different modelling



176 constraints. The second ice thickness distribution is the dataset of Langhammer et al. (2019), hereafter referred to
177 as THIL. This distribution was produced by combining measured ice thicknesses (41 helicopter borne GPR profiles
178 with a total of 53247 points measured in 2017) and modelling constraints with the Glacier Thickness Estimation
179 (GlaTE) inversion scheme. We correct both datasets for glacier geometry changes to refer to the glacier state in
180 2018, 2019 and 2020 respectively by subtracting the amount of local surface lowering. This concerns the local
181 height difference between the UAV created DSMs of 2018-2019-2020 and the DEM used for the respective ice
182 thickness datasets. The latter are two DEMs provided by SwissTopo. DHM25 valid for 1991 (used for THIZ) and
183 SwissALTI3D valid for 2015 (used for THIL).

184

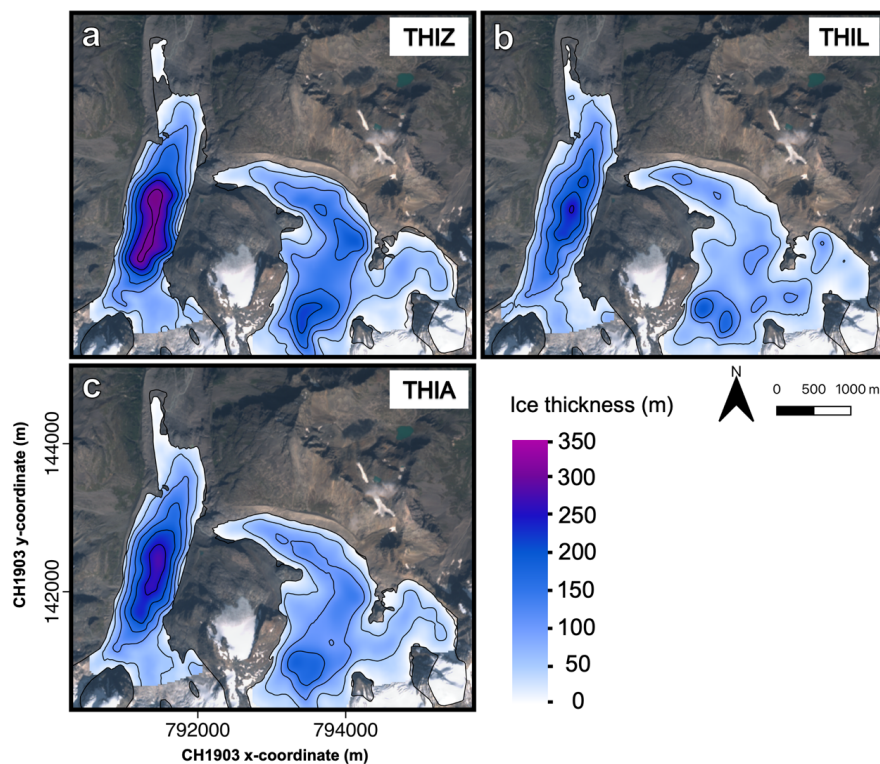
185 Although both ice thickness distributions (Figure 3a and Figure 3b) have a similar pattern (location of
186 overdeepenings, location of maximum ice thickness), large local differences exist. The ice thickness maximum for
187 instance occurs at a similar location but is about 310 m for THIZ and 250 m for THIL. This corresponds to a
188 difference of 15-20% which is however still within the error bounds of the datasets. Conversely, there are also
189 certain zones (especially higher up Vadret da Morteratsch) where the difference between the two datasets is more
190 than 150 metres.

191

192 Because of the significant differences between both ice thickness distributions, we hypothesize that the choice for
193 a particular distribution can have a major influence for the calculations in this study. To verify the maximum ice
194 thickness of Vadret da Morteratsch, we measured the ice thickness once again at the thickest point in 2020 with a
195 Narod Radio Eco Sounding (RES) system, similar to Van Tricht et al. (2020). We preferred to use a low frequency
196 of 5 MHz to limit the amount of attenuation due to disturbances in the glacier such as water inclusions, repeatedly
197 observed during the fieldwork. We found a maximum value of 296 metres which is relatively close to the
198 maximum thickness from the THIZ dataset. We can therefore certainly not ignore this dataset, despite the smaller
199 number of measurements and the older date of creation. Therefore, for further calculations, we decided to use the
200 mean ice thickness from THIZ and THIL at every grid cell, hereafter referred to as THIA (Figure 3c). The effect
201 of using THIA, as opposed to relying on THIZ or THIL, is examined as a part of the sensitivity analysis (section
202 5.3). For the areas where the current elevation is lower than the bedrock inferred from THIZ and THIL, and where
203 there is no ice as a result, we assume a minimal ice thickness of 5m as in Zekollari et al. (2013).

204

205



206

207

208 **Figure 3.** Ice thickness distribution of the ablation area of the Morteratsch-Pers glacier complex in 2020. (a) THIZ (ice
209 thickness distribution of Zekollari et al. (2013), (b) THIL (ice thickness distribution of Langhammer et al. (2019) and (c) THIA
210 (average ice thickness distribution). Contour lines represent 50 m intervals. Note that at the front of Vadret da Morteratsch
211 and locally at the front of Vadret Pers, the glacier outline is larger than the ice thickness dataset. The current surface elevation
212 of these areas is lower than the bedrock elevation inferred from THIL and THIZ. The background image is a Sentinel-2 true
213 colour composite satellite image from 13 September 2020.

214

215

216 3 Methods

217

218 3.1 Continuity-equation method

219

220 The continuity equation for glacier flow with constant density (Eq. 1) links the local mass balance (b) and the ice
221 flux divergence per unit width in the local vertical ice column ($\nabla \cdot \vec{q}$) with local changes in the ice thickness ($\frac{\partial H}{\partial t}$),
222 all expressed in metres of ice equivalent per year (m i.e. yr^{-1}) (see e.g. Hubbard et al., 2000; Berthier and Vincent,
223 2012).

224

225



226
$$\frac{\partial H}{\partial t} = b - \nabla \cdot \vec{q}$$
 (1)

227

228

229 Eq. 1 shows that the difference between the local mass balance and ice flux divergence must be compensated by
230 a change in local ice thickness. If the bedrock elevation is assumed to be constant and compaction is negligible,
231 which is the case in the ablation area (with ice throughout the entire column), the local ice thickness (H) in Eq. 1
232 can be replaced by the elevation of the surface (h). Further, because basal and internal mass balance in the ablation
233 area are predominantly much smaller compared to the surface mass balance (b_s) (Kaser et al., 2003; Huss et al.,
234 2015), b can be replaced by b_s , which after a reorganisation leads to the following expression:

235

236

237
$$b_s = \frac{\partial h}{\partial t} + \nabla \cdot \vec{q}$$
 (2)

238

239

240 By determining the local elevation changes (section 3.2) and the components that make up for the ice flux
241 divergence per unit width (from now on referred to as ice flux divergence; sections 3.3-3.6), the SMB pattern can
242 then be derived.

243

244

245 **3.2 DSM generation and surface elevation changes ($\partial h/\partial t$)**

246

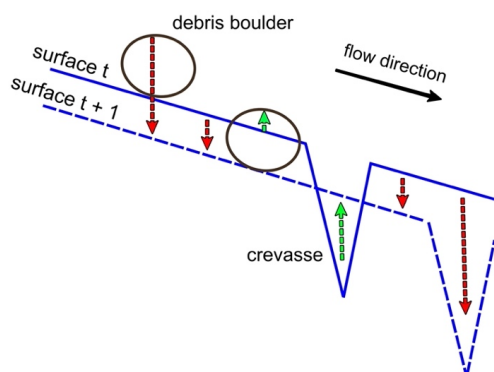
247 First, all the data from the UAV surveys are used to generate DSMs on a common local coordinate system (CH1903
248 LV03). All the images collected during the UAV surveys are processed into orthophotos and DSMs using the
249 photogrammetry workflow implemented in Pix4D. The accuracy of the reconstructed DSMs is assessed using
250 ground validation points (GVPs), which are GCPs that are not used to georeference the project. Subsequently,
251 surface elevation changes are directly computed from these DSMs by subtracting the DSMs from each other (2018-
252 2017, 2019-2018, 2020-2019). Initially, all the DSMs are generated with a very high resolution of 0.05-0.10 m.
253 But eventually, the surface elevation changes are resampled to 25 m resolution for further calculations using a
254 block moving average filter. This corresponds to the resolution of the ice thickness datasets and will therefore be
255 the grid size for all of the following calculations.

256

257 A commonly observed feature on surface elevation change maps derived from high resolution DSMs are
258 alternating positive and negative differences. These are caused by the advection of local glacier topography such
259 as crevasses, moulins and large ice or rock boulders (Figure 4) (Rounce et al., 2018; Yang et al., 2020). The above-
260 mentioned variations are not caused by reduced or increased melt or accumulation and therefore need to be filtered
261 out in order to make a correct SMB estimate.

262

263



264

265

266 **Figure 4.** The advection of surface topography (such as debris boulders and crevasses) can alter surface elevation changes
 267 between timestep t and $t+1$ (red = negative $\partial h/\partial t$, green = positive $\partial h/\partial t$). The net effect on the surface elevation depends on
 268 the amount of lowering and the vertical extent of the moving features on the glacier surface.

269

270

271 To filter out these variations, we apply a block moving average filter (Eq. 3) with a window size d (in number of
 272 grid cells) which is the product of a smoothing parameter (k) and the local surface velocity (u_s) (Eq. 4).

273

274

$$275 \frac{\partial h}{\partial t} [x,y] = \frac{1}{(2d+1)^2} \left(\sum_{i=-d}^d \sum_{j=-d}^d \frac{\partial h}{\partial t} [x+i,y+j] \right) \quad (3)$$

276

$$277 d = k * \text{round}\left(\frac{u_s}{25}\right) \quad (4)$$

278

279

280 x and y are Cartesian coordinates, and i and j are indices. In contrast to a block moving average filter with constant
 281 width, the surface elevation changes are only smoothed in areas where the glacier is flowing. In areas where the
 282 glacier is (almost) stagnant, $\partial h/\partial t$ variations are kept as these cannot have been caused by the movement. Hence,
 283 $\partial h/\partial t$ is not modified when d is smaller than one, implying that the local glacier movement during a year was
 284 smaller than the grid resolution (see Eq. 3 and Eq. 4). In order to investigate the optimal distance over which the
 285 surface elevation changes need to be smoothed, k is varied between 0 (no modification) and 10. Ideally, k should
 286 not be taken too large to avoid eliminating all variations, including SMB induced variations.

287

288

289 3.3 Horizontal surface velocity

290

291 Glacier surface velocities, which are needed to calculate the ice flux divergence (section 3.4) and to smooth the
 292 surface elevation changes (section 3.2), are computed for the three individual mass balance years. Velocity grids



293 are derived by applying the Image Geo Rectification and Feature Tracking toolbox (ImGRAFT), an open-source
294 tool in MATLAB (Messerli and Grinsted, 2015). Instead of using visual image data with variable illumination and
295 snow cover, the feature tracking algorithm is run on hillshades (relief DSMs) of the original DSMs resampled to
296 a resolution of 2 m (Messerli and Grinsted, 2015). The latter turned out to improve the correlation success (Rounce
297 et al., 2018).

298

299 Velocity maps are computed and corrected for differences in acquisition dates to obtain values in metre per year.
300 Then, a series of filters is applied to the output of the cross-correlation to exclude poorly correlated pixels and
301 those with unrealistic displacements or flow directions (Ruiz et al., 2015). The latter is a common issue for snow
302 covered areas or debris covered areas where no accurate displacements can be detected. As a first filter, all the
303 computed velocity vectors outside the glacierized areas are removed by using the digitized glacier outlines (Heid
304 and Kääb, 2012). Then, a median filter is applied which removes velocity vectors that deviate too much from the
305 surrounding vectors (Heid and Kääb, 2012; Nagy et al., 2019). Finally, we also impose a maximum velocity
306 threshold derived from the modelled velocities in Zekollari et al. (2013), which are constrained with field
307 observations. In other words, we limit the maximum surface velocity at every grid cell to the velocity modelled in
308 Zekollari et al. (2013) + 20%. The latter is a margin to take into account potential errors present in the study of
309 Zekollari et al. (2013). However, after analysis this proved not to be necessary as these high values did not occur.
310 The raw velocity maps containing gaps after filtering are then interpolated using a spline interpolation (Ruiz et al.,
311 2015). As validation, we compare the obtained velocities with measured velocities from stakes.

312

313

314 **3.4. Ice flux divergence from ice thickness and surface velocities**

315

316 The ice flux divergence (in m i.e. yr⁻¹) corresponds to the local upward or downward flow of ice relative to the
317 glacier surface. It represents the difference between the ice supplied from upstream and lost downstream at a
318 particular position. It is defined to be negative for upward motion (mass supplied to the surface, also referred to as
319 the emergence velocity) and positive for downward motion (mass is removed from the surface, also referred to as
320 the submergence velocity).

321

322 Different approaches exist to calculate the ice flux divergence ranging from the use of 3D ice flow models
323 (Seroussi et al., 2011; Vincent et al., 2020) to the use of simple geometric calculations and flux gates (Nuimura et
324 al., 2011; Berthier and Vincent, 2012). The important distinction is the simplicity and the resolution with which
325 they can be calculated. In this study, the ice flux divergence is computed for each grid cell, by combining surface
326 velocities and ice thickness according to Eq. 5:

327

328

$$329 \nabla \cdot \vec{q} = F \left(u_{s,x} \frac{\partial H}{\partial x} + u_{s,y} \frac{\partial H}{\partial y} + H \frac{\partial u_{s,x}}{\partial x} + H \frac{\partial u_{s,y}}{\partial y} \right) \quad (5)$$

330

331



332 The right side of Eq. 5 contains two horizontal ice flux components of which the first corresponds to the ice
333 thickness divergence and the second one to the velocity divergence (Reeh et al., 2003). Both are computed from
334 the relevant derivatives. F is the depth averaged glacier velocity ratio (\bar{u}/u_s). For an isothermal glacier, with
335 negligible basal sliding and Glen's flow coefficient $n = 3$, F is 0.8. However, the Morteratsch-Pers glacier complex
336 is assumed to be a temperate alpine glacier complex which is accompanied by basal sliding. According to Zekollari
337 et al. (2013), internal deformation accounts glacier wide on average for 70% of the flow and basal sliding for the
338 remaining 30%. However, in the ablation area the contribution of internal deformation is most likely even higher.
339 Therefore, for the standard runs in this study, we take an F -value of 0.9. However, the F -value may vary locally
340 (Zekollari et al., 2013) and varying this parameter will therefore be part of the sensitivity analysis.

341
342

343 3.4 Spatial scales of the ice flux divergence

344

345 In contrast to the surface elevation changes, for which the accuracy is expected to be high, the computed ice flux
346 divergence is subject to larger uncertainties. This uncertainty directly relates to the large uncertainties in the
347 reconstructed ice thickness field. Moreover, a considerable part of the uncertainty also originates from the spatial
348 scales that need to be considered: due to longitudinal stresses, the local ice dynamics do not only depend on the
349 local glacier geometry (an assumption of the Shallow Ice Approximation, see e.g. Hutter and Morland (1984)),
350 but also on the surrounding geometry, typically over scales corresponding to several times the local ice thickness
351 (accounted for in higher-order and Full Stokes models, see e.g. Zekollari et al. (2014), where such a model was
352 applied for this glacier complex). Local gradients of the ice thickness and the velocity are often magnified when
353 they are determined on a numerical grid with a central difference scheme. This is directly reflected in the ice flux
354 divergence pattern. Therefore, to make the ice flux divergence solution independent of the resolution and to take
355 non-local stresses into account, larger scales must be considered (Reeh et al., 2003; Rounce et al., 2018). In studies
356 applying the continuity equation on larger glaciers or ice sheets, it is usually sufficient to resample the ice flux
357 divergence grid to a much lower resolution (Nuimura et al., 2011; Vincent et al., 2016; Rounce et al., 2018).
358 However, as we aim for a high resolution of the SMB determination in this study, we opt to retain the 25 m
359 resolution and to consider larger scales for the calculation of the ice flux divergence.

360

361 Different filters have been applied, of which most are constant box filters (e.g. mean, median) with a strong
362 variation in size (up to 10000 metres) (Kääb and Funk, 1999; Seroussi et al., 2011; Rounce et al., 2018). Such
363 filters give equal weights to cells within the box irrespective of their distance from the point in consideration
364 (Kamb and Echelmeyer, 1986; Le Brocq et al., 2006). Also, these filters have an abrupt cut-off point where the
365 weighting becomes zero (Le Brocq and others, 2006). Furthermore, effects of perturbations in for example ice
366 thickness have been demonstrated to fade out exponentially for ice flow (Kamb and Echelmeyer, 1986). Because
367 of all these reasons, we apply a local exponential decay filter here (Eq. 6):

368
369

$$370 \nabla \cdot \bar{q}_{[x,y]} = \sum_{i=-\text{dist}}^{\text{dist}} \sum_{j=-\text{dist}}^{\text{dist}} W_{[x+i,y+j]} \nabla \cdot \bar{q}_{[x+i,y+j]} \quad (6)$$

371



372

373 Here, $dist$ is the maximum distance of a cell which is taken into account in the exponential decay filter (set at 2.5
374 km), i and j are indices, and W represents the weight of a particular cell at position $[x+i, y+j]$ (Le Brocq et al.,
375 2006):

376

377

$$378 \quad W_{[x,y]} = e^{-\frac{1}{sl} \sqrt{(x'-x)^2 + (y'-y)^2}} \quad (7)$$

379

380

381 In Eq. 7, x and y are the coordinates of the point being filtered while x' and y' are the coordinates of the weighted
382 points, sl is the scaling length and is a crucial parameter determining how fast the exponential filter fades. This
383 parameter directly relates to the length scale over which the longitudinal stresses determine the local ice flow.
384 Theoretically, this scaling length is in the range of 1-3 times the local ice thickness for valley glaciers and 4-10
385 times for ice sheets (Kamb and Echelmeyer, 1986; Le Brocq et al., 2006). For our experiments, we vary the scaling
386 length depending on A times the local ice thickness (Eq. 8). In this way, we incorporate variations within the study
387 area into the exponential decay filter and we account for non-local flow coupling. The latter was shown to be an
388 improvement compared to fixed-size filters (Le Brocq et al., 2006). In this way, the ice flux divergence in areas
389 with a larger ice thickness is considered over a larger distance compared to areas with a smaller ice thickness.

390

391

$$392 \quad sl[x, y] = A * H[x, y] \quad \text{with } A \in \{0: 1: 10\} \quad (8)$$

393

394

395 To determine the optimal procedure to include the effects of (longitudinal) stresses and uncertainty in the input
396 data, we perform multiple experiments with the exponential decay filter. For this, we examine whether (i) the ice
397 flux divergence, (ii) the gradients of velocity and ice thickness or (iii) both should be considered over larger spatial
398 scales for optimal results in the determination of the SMB.

399

400 First, the ice flux divergence is considered over larger spatial scales by applying the exponential decay filter to the
401 ice flux divergence field. Second, to compensate solely for the effects of large gradients, the gradients are
402 considered over larger spatial scales. We therefore apply the exponential filter to the ice thickness and velocity
403 gradients and calculate the ice flux divergence using these smoothed gradients. Third, to compensate for the
404 negative effects of very large scaling lengths for both previous experiments and the biases related to both, we filter
405 twice. Hence, both filters are applied after each other. In this way, the smoothness of the ice flux divergence field
406 increases while the top values are not damped as much as applying a filter once with a long scaling length. Filtering
407 twice is essentially similar to first resampling to a lower resolution and then applying one filter. Earlier research
408 did not require such filtering to be applied due to a much coarser resolution (Seroussi et al., 2011; Rounce et al.,
409 2018). For every experiment, the modelled and measured SMB values at the position of the stakes are compared
410 (see section 2.2). As metrics to quantify the performance of the procedure, the mean absolute error (MAE) and the
411 root mean square error (RMSE) are used (Eq. 9 and 10). The MAE is defined as the absolute difference between



412 the modelled and the measured SMB. The RMSE on the other hand takes into account the variance of the errors.
 413 n is the number of stake measurements. The uncertainty of the SMB measurements is estimated to be ± 0.2 m i.e
 414 yr^{-1} and is also taken into account in the analysis. More specifically, for each filter option we carry out 100 versions
 415 in which we perturb the measured SMB. This is done by randomly adding a value between -0.2 and 0.2 distributed
 416 around 0. Then, for the option under consideration, the average MAE and RMSE are calculated from Eqs. 9 and
 417 10, where n is the number of SMB measurements for every year which is 16, see section 2.2. i is an index ranging
 418 from 1 to n (16), x_i and y_i are the Cartesian coordinates of the different stakes under consideration.

419 .
 420
 421

$$422 \text{MAE} = \frac{1}{n} (|\sum_{i=1}^n b_{s,\text{modelled}}(x_i, y_i) - b_{s,\text{measured}}(i)|) \quad (9)$$

423

$$424 \text{RMSE} = \sqrt{\frac{\sum_{i=1}^n (b_{s,\text{modelled}}(x_i, y_i) - b_{s,\text{measured}}(i))^2}{n}} \quad (10)$$

425
 426

427 4 Results

428

429 4.1 Surface elevation changes and filtering

430

431 The accuracy of the elevation product is assessed by comparing the photogrammetrically created DSMs with
 432 GVPs, randomly divided over the study area. Mean absolute errors (MAE) between measured and modelled
 433 elevation are in the order of a few cm (Table 2), which is similar to values found in other studies (Whitehead et
 434 al., 2013; Immerzeel et al., 2014; Wigmore and Mark, 2017; Zhang et al., 2019). As such, the accuracy of the
 435 created DSMs is high. Furthermore, the mean error (ME) is close to zero which indicates that the created DSMs
 436 are not biased. For 2017, the slightly larger MAE is probably caused by a smaller number of GCPs combined with
 437 a reduced visual content because of fresh snow on the glacier surface. Further, the small MAE and RMSE of the
 438 DSM in 2020 highlight the advantage of using a RTK equipped with an RTK GPS (P4RTK) for which a smaller
 439 amount of GCPs is needed to reach similar or better accuracies compared to a classic setup (UAV without RTK
 440 correction).

441

442 **Table 2.** Mean absolute error (MAE) and root mean square error (RMSE) of the elevation differences between the DSMs and
 443 the GVPs in different years. (Units are in m).

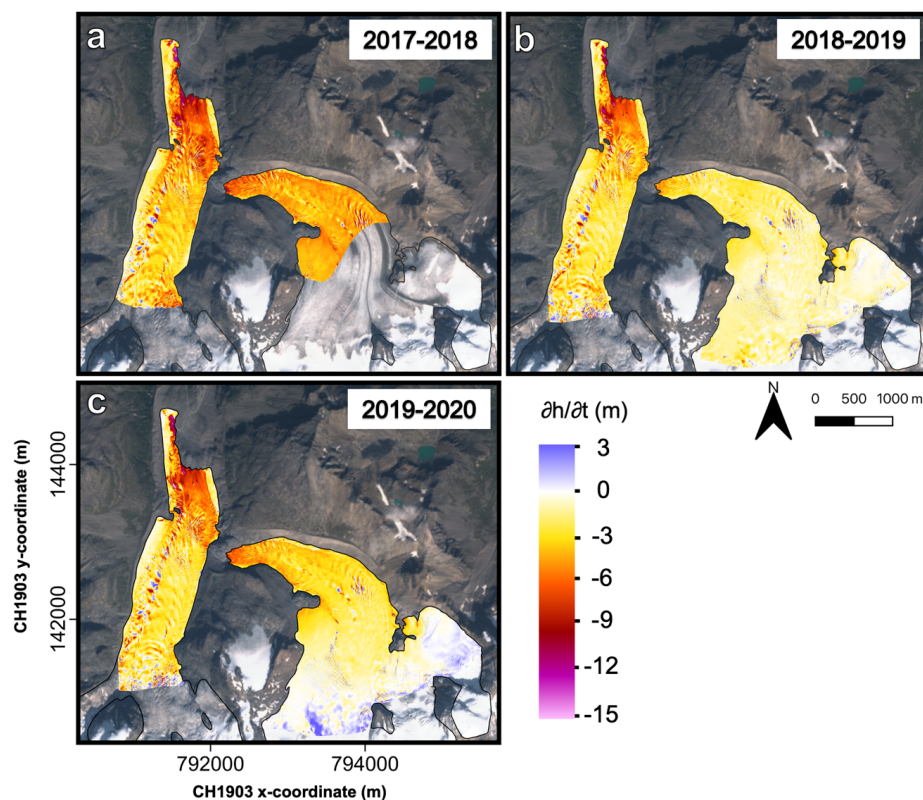
444

Year	MAE	ME	RMSE	GCP density (km ⁻²)	UAV used
2017	0.09	-0.07	0.16	11	P4PRO
2018	0.06	-0.02	0.22	24	P4PRO
2019	0.08	0.03	0.16	18	P4PRO
2020	0.07	0.03	0.10	11	P4RTK

445



446 The different maps for the three balance years, display a very detailed pattern of surface elevation changes (Figure
447 5). For example, alternating positive and negative surface elevation changes are noticeable and can be explained
448 by the advection of local glacier surface topography due to glacier movement (see also Figure 4). In addition,
449 significant less negative $\partial h/\partial t$ values at the left side of Vadret da Morteratsch, especially where the glacier
450 protrudes towards the north, are likely the result of a debris cover insulating the ice below and decreasing the
451 melting rate (Reznichenko et al., 2010; Rounce et al., 2018). Given that the ice fluxes can be assumed to remain
452 relatively constant over the three years in consideration, the elevation changes indicate that 2017-2018 was the
453 year with the most negative SMB (which is confirmed by field measurements, see e.g. Fig. 12). Further, large
454 positive surface elevation changes can be distinguished for 2019-2020 at the highest part of Vadret Pers. This is
455 probably the result of avalanches originating from the steep accumulation area and persistent snow cover in these
456 areas. This is striking as surface elevation changes further down on the glacier are generally more negative
457 compared to 2018-2019: i.e. the SMB gradient on Vadret Pers is steeper in 2019-2020 compared to 2018-2019.
458
459



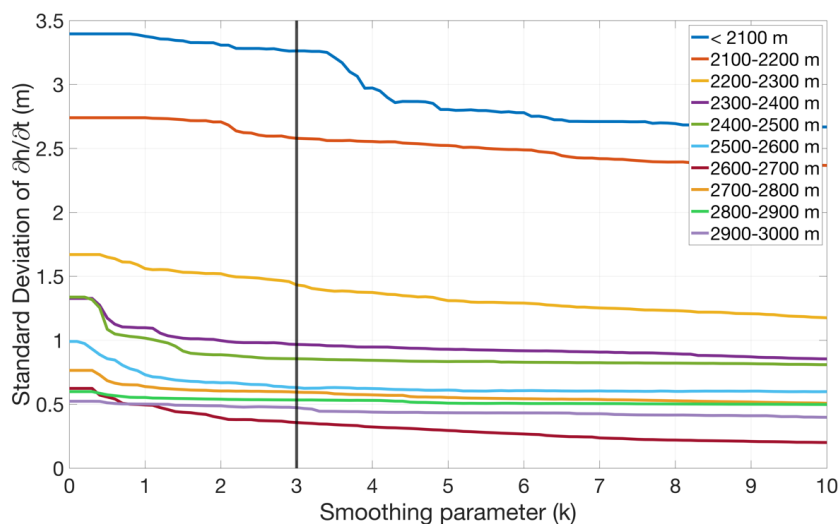
460
461
462
463
464

Figure 5. Surface elevation changes for (a) 2017-2018, (b) 2018-2019 and (c) 2019-2020. The spatial resolution is equal to 8 cm. The outline of the glacier corresponds to the latest year of observation for every balance year in consideration. The background image is a Sentinel-2 true colour composite satellite image from 13 September 2020.



465
466
467
468
469
470
471
472
473
474
475
476
477

Alternating positive and negative surface elevation changes are occurring, caused by the advection of surface topography (Figure 4 and Figure 5). We remove these non-SMB features by applying a block moving average filter over a distance that is determined by the local surface velocity (see section 3.2). When the smoothing parameter (k-value) is increased, the standard deviation (SD) within elevation bands of 100 m decreases significantly for all elevation intervals above 2300 m (Figure 6). This means that the variation is considerably reduced within these bands. The largest decrease is for k-values between 0 and 1 but only from a k-value of 3 onwards, an almost complete levelling out of the SD can be noticed. In addition, it is clear that the SD remains generally above 0.5 m. This is due to variations within the elevation bands that are preserved, for example caused by elevation differences.



478
479

Figure 6. The surface elevation changes are smoothed using a block moving average filter over a distance depending on the local surface velocity and a smoothing parameter (k) between 0 and 10. The different lines represent the standard deviation (m) of the surface elevation changes within elevation bands of 100 metres. The vertical black line indicates the chosen parameter of $k = 3$.

484
485
486
487
488
489
490

Further, for the elevation bands below 2300 metres, the SD remains higher and decreases more slowly or even not at all. These elevation bands concern the lowest, slow flowing glacier areas of Vadret da Morteratsch. Here, variations in surface elevation changes are not related to the advection of surface topography and are correctly kept (not smoothed). The variations in this area are for example caused by differential melting due to debris. If a constant box filter would have been used, this would have resulted in the surface elevation changes in these areas



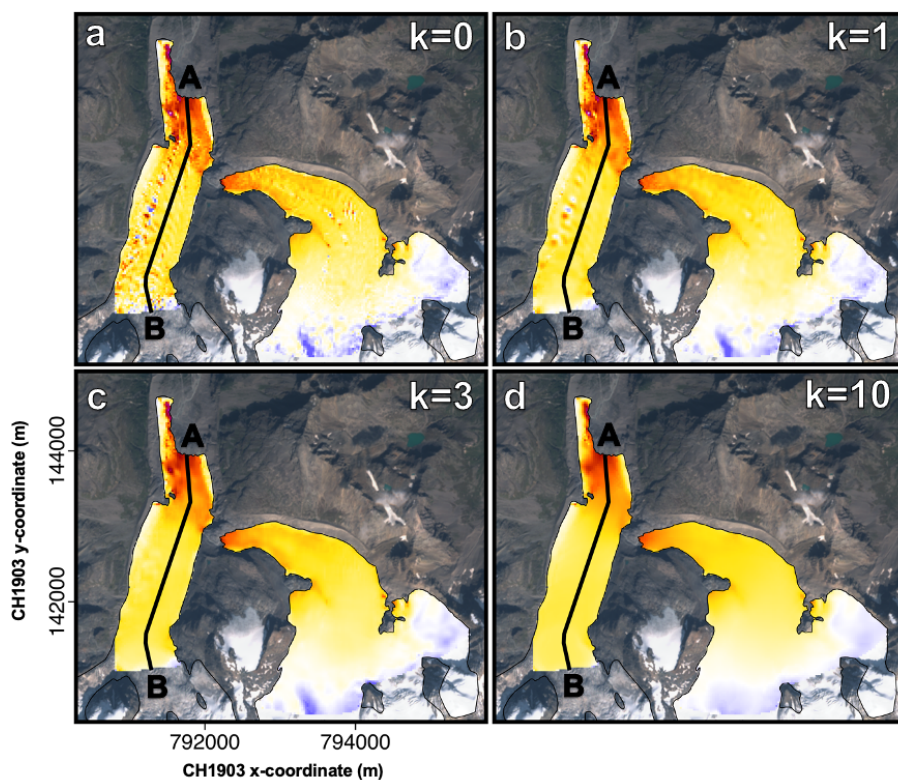
491 to be smoothed to the same extent. This would imply that actual SMB caused patterns would no longer be visible,
492 which highlights the advantage of using a filter with a window size depending on the local surface velocity.

493

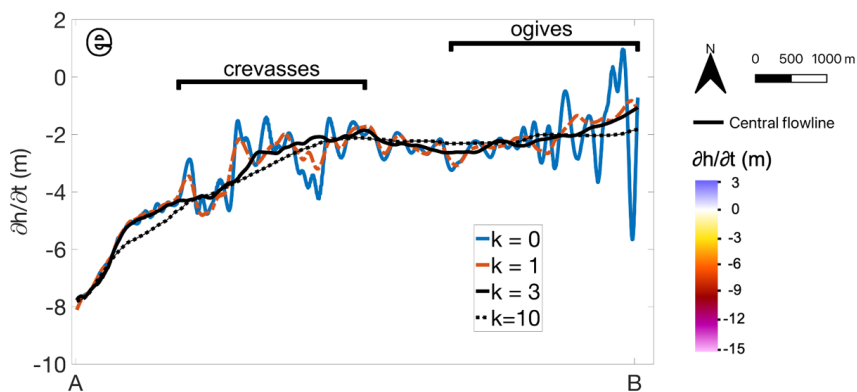
494 For $k=1$, there remain a lot of patches with surface elevation changes arising from the glacier movement (Figure
495 7). This is significantly less when k equals 3. If k were to be enlarged further, for example to $k=10$, the pattern of
496 $\partial h/\partial t$ fades completely. The positive surface elevation changes in the upper area of Vadret Pers are for example
497 completely smeared out. It is therefore essential to minimise the window size of the block filter so that variations
498 owing to glacier movement are eliminated without losing too much detail. For all these reasons, we choose k to
499 be equal to 3 for further calculations.

500

501



502



503

504

505 **Figure 7.** Surface elevation changes between 2019 and 2020, smoothed using a moving average filter and a smoothing
 506 parameter (k) of 0 (panel a), 1 (panel b), 3 (panel c) and 10 (panel d). The black line represents an approximation of the central
 507 flowline of Vadret da Morteratsch. The background image is a Sentinel-2 true colour composite satellite image from 13
 508 September 2020. The graph (panel e) shows the surface elevation changes along the central flowline indicated in panels a, b,
 509 c, and d and some distinct topographical features which need to be filtered out.

510

511



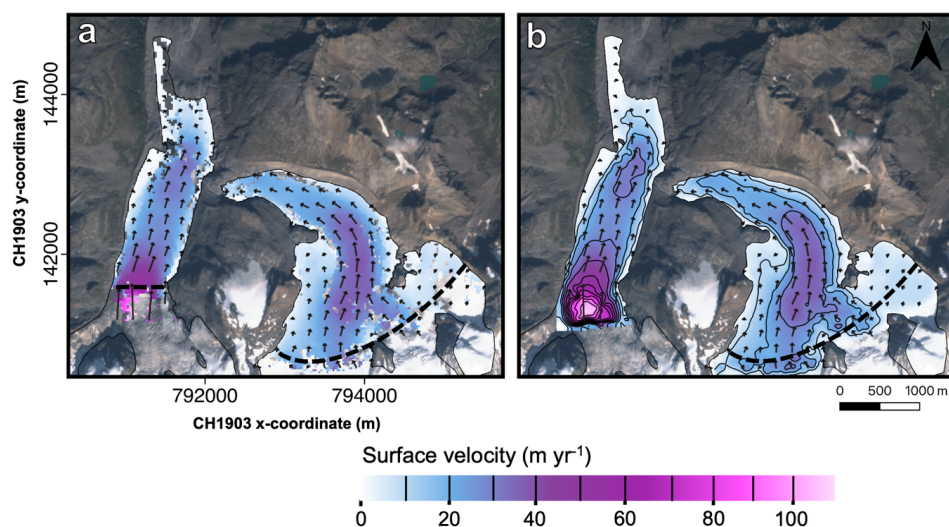
512 **4.2 Glacier surface velocity**

513

514 The velocity map derived from feature tracking and filtered for errors (see section 3.3), contains several voids
515 (Figure 8a). This is caused by a lack of correlation between the two years, which is typically related to deformations
516 of the surface and the presence of snow cover or debris. The latter hampers an accurate tracking between two
517 consecutive years. To fill these gaps, spline interpolation is used (Figure 8b).

518

519



520

521

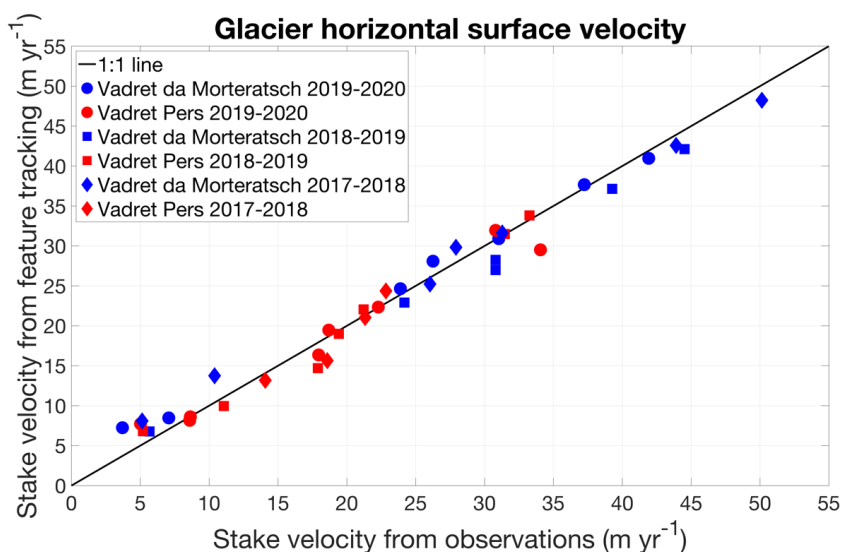
522 **Figure 8.** Horizontal surface velocities derived from feature tracking between 2019 and 2020. (a) filtered surface velocity, (b)
523 void-filled filtered surface velocity. The black arrows indicate the flow direction. The dashed black line indicates the limit of
524 the glacier area where the velocity is modelled without many gaps (area used for further analyses, e.g. when calculating ice
525 flux divergences). The background image is a Sentinel-2 true colour composite satellite image from 13 September 2020. The
526 contour lines are added for every 10 m and they are indicated in the colorbar.

527

528

529 Comparison with the velocities obtained by field measurements using ablation stakes (based on high-precision
530 RTK GPS system, estimated accuracy of approx. 0.1 m yr^{-1}) reveals a good agreement. We find the ME and RMSE
531 to be $0.01 / 1.7 \text{ m yr}^{-1}$ for 2017-2018, $0.99 / 1.9 \text{ m yr}^{-1}$ for 2018-2019 and $-0.37 / 1.8 \text{ m yr}^{-1}$ for 2019-2020 (Figure
532 9).

533



534

535

536 **Figure 9.** Comparison between surface velocities at stakes from field observations (high precision GPS measurement at stakes)
537 and from feature tracking.

538

539

540 The surface velocities of 2017-2018 are higher compared to 2018-2019. This might be caused by the slowdown
541 of the glacier's ablation tongue, commonly observed in mountain valley glaciers as a result of glacier thinning
542 (Dehecq et al., 2019). However, because the surface velocities in 2019-2020 also appear to be slightly larger
543 compared to 2018-2019, it might be due to a larger amount of basal sliding. The latter can be caused by an increased
544 supply of meltwater lubricating the glacier's base which can be linked to a more negative $\partial h/\partial t$ in 2017-2018 and
545 2019-2020 compared to 2018-2019 (see also Figure 5).

546

547

548 4.3 Ice flux divergence

549

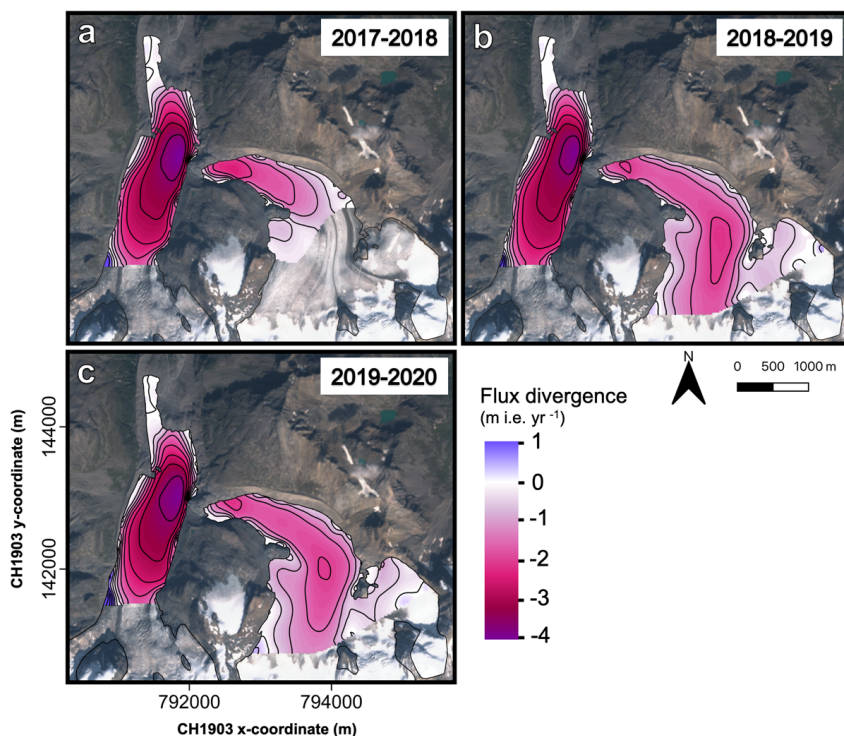
550 After considering various spatial scales and filter procedures to determine the ice flux divergence, we find optimal
551 results (lowest MAE, RMSE and minimal scaling length, see section 5.2) when both filters are applied after each
552 other for a scaling length of $4xH$ to smooth the ice thickness and velocity gradients and a scaling length of $1xH$ to
553 smooth the ensuing ice flux divergence (see section 4.3). These values are close to the theoretical values of the
554 fundamental longitudinal scaling length for valley glaciers, mentioned in Kamb and Echelmeyer (1986). It shows
555 that the data needs to be considered over large spatial scales which implies that the ice flux divergence field must
556 be sufficiently smooth to give accurate results.

557

558 The computed ice flux divergence is clearly characterized by negative values over both glacier tongues (Figure
559 10). This represents horizontal compression and associated vertical extension which is generally expected for



560 ablation areas (e.g. Kääb and Funk, 1999). This horizontal compression translates into an ice supply towards the
561 surface (emergence velocity), which counters the effect of the negative mass balance on the local ice thickness
562 change (and neutralizes it in case the glacier is in equilibrium with the local climatic conditions). The ice flux
563 divergence reaches a minimum between 500 and 1000 m from the terminus of the Vadret da Morteratsch with
564 values close to 4 m i.e. yr⁻¹ (Figure 10). In this area, both the ice thickness (Figure 3) and the surface velocity
565 (Figure 8) decrease significantly which leads to large negative gradients and hence upward motion (negative ice
566 flux divergence). It is therefore not surprising that there is a complex pattern of transverse crevasses in this area
567 (see Figure 2). The maximum ice flux divergence at the eastern side of Vadret da Morteratsch near the former
568 confluence area with Vadret Pers is suspicious. This is likely caused by the very large ice thickness gradient as a
569 result of underestimated ice thickness in the THIZ dataset. In this area, the THIZ dataset revealed zero ice thickness
570 as a result of an overestimation of the bedrock elevation (Figure 3).
571
572



573
574
575 **Figure 10.** Maps of the modelled ice flux divergence for the different years under consideration. Contours are added for every
576 0.5 metre per year. The background image is a Sentinel-2 true colour composite satellite image from 13 September 2020.
577
578
579



580

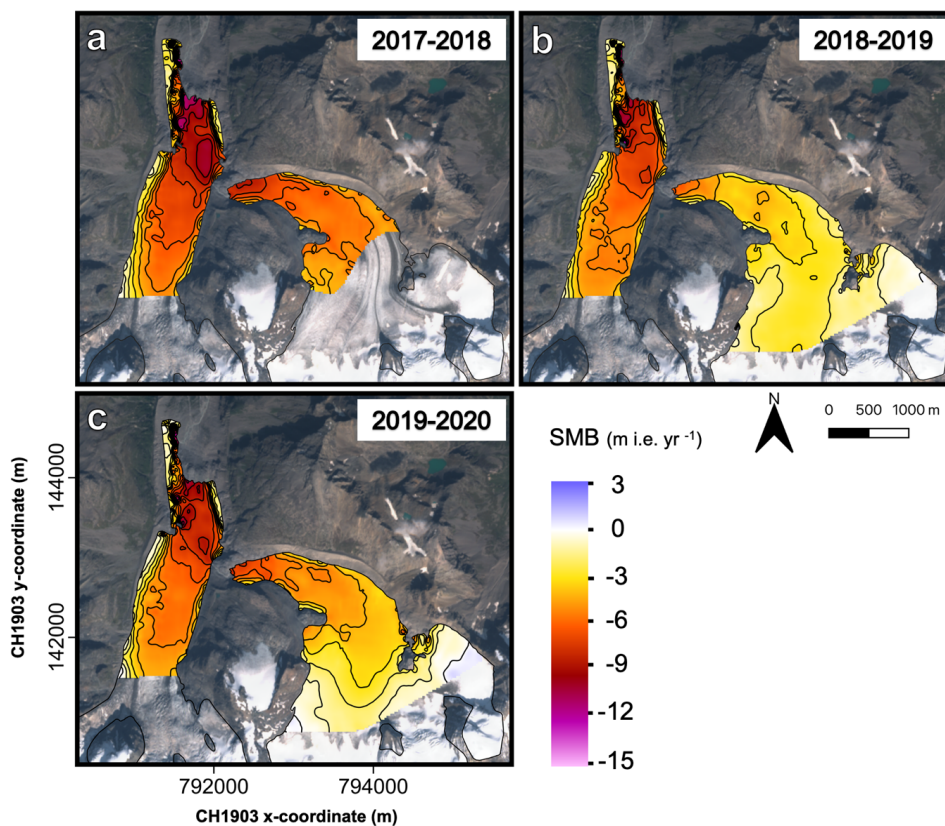
581 4.4 SMB from UAV

582

583 The final step of the method is to add the surface elevation changes (see Figure 5 and Figure 6) and the computed
584 ice flux divergence (Figure 10) to obtain the SMB (see Eq. 1). The final product, the modelled SMB for the three
585 balance years, is shown in Figure 11. The three years in consideration clearly show a similar pattern. Areas with a
586 less negative SMB are located at the same locations (e.g. western margin of Vadret da Morteratsch). Areas with
587 the most negative SMB are also at the same location (e.g. glacier fronts). The ice flux divergence is prominently
588 not able to compensate for the very negative SMB so that there is net mass loss everywhere and the altitude changes
589 are less than zero. The most negative SMB (up to $-13 \text{ m i.e. yr}^{-1}$) is found at the front of Vadret da Morteratsch in
590 2017-2018 which is in accordance with the SMB measurements. This concerns the lowest area which is also quasi-
591 stagnant with a very limited supply of ice from upstream (see Figure 10).

592

593



594

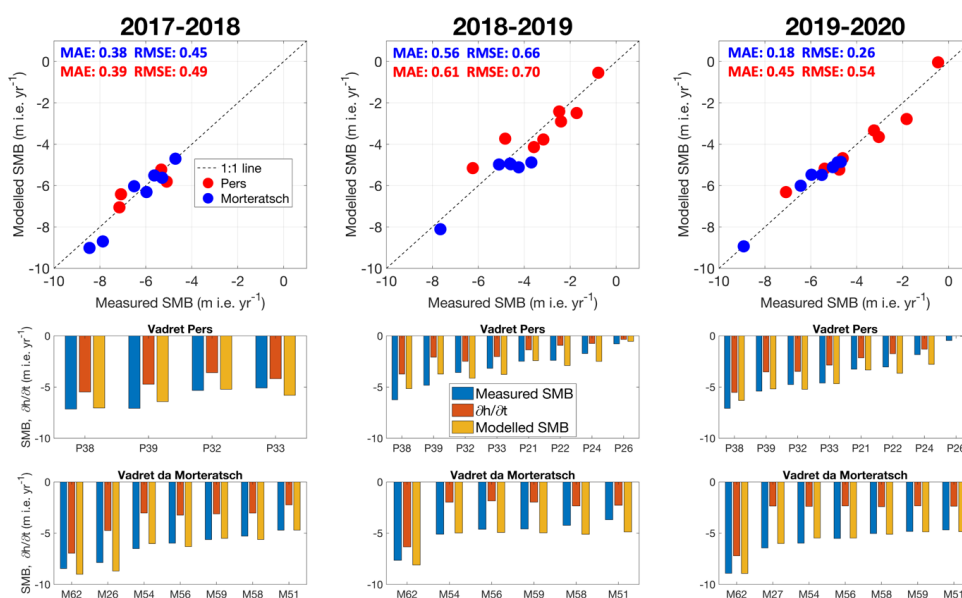
595

596 **Figure 11.** Maps of the modelled SMB fields. Contours are added for every metre per year. The background image is a Sentinel-
597 2 true colour composite satellite image from 13 September 2020.



598
 599
 600
 601
 602
 603
 604
 605
 606
 607
 608

The associated point-by-point comparison between modelled and measured SMB confirms the good match with deviations generally smaller than $0.5 \text{ m i.e. yr}^{-1}$ (Figure 12). The largest differences are found at the front of Vadret Pers (Figure 12). Near the glacier front, the ice flux divergence is likely underestimated as a result of overestimated ice thickness in this area of the THIZ dataset. The latter decreases the ice thickness gradient in this area. Stake M26 (see Figure 2) is excluded from the analysis because it was located in the middle of a field of transverse crevasses during the survey in 2018. This location might be associated with increased ablation because the stake was located on the top of a serac.



609
 610

Figure 12. Point-by-point comparison of modelled and measured SMB. In the lower panels, the difference between the modelled SMB (yellow bar) and the local elevation change (red bar) results from the modelled ice flux divergence. The labels refer to the stake names as used in the fieldwork programme. The MAE and RMSE of the modelled SMB are added in the upper panels (Values are in m i.e. yr^{-1}).

615
 616
 617
 618
 619
 620
 621
 622

The MAE and RMSE for the optimal SMB fields are well below 1 m i.e. yr^{-1} with a minimum of $0.18 \text{ m i.e. yr}^{-1}$ for Vadret da Morteratsch in 2019-2020 (Figure 12). The MAE and RMSE are somewhat larger for Vadret Pers with a maximum of $0.61 \text{ m i.e. yr}^{-1}$ in 2018-2019 which is mainly caused by the larger deviation for the lowest two stakes (Figure 12).



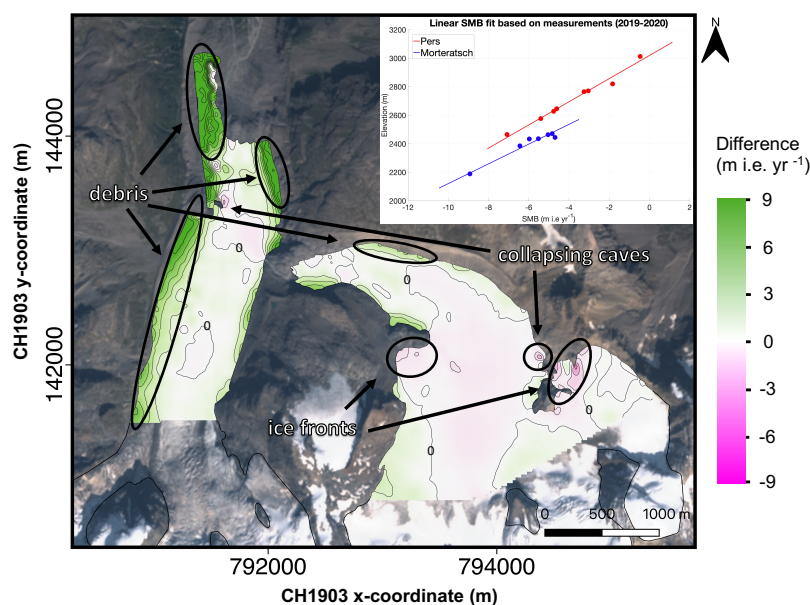
623 4.5 Lateral variations in the SMB pattern

624

625 Using the continuity method based on close-range (UAV) remote sensing data clearly reveals a much more detailed
626 picture of SMB than is possible from a stake network on a limited number of locations. This is evident in the
627 lateral heterogeneity of SMB, which is often overlooked when considering elevation as the prime variable to plan
628 the stake locations. In Figure 13 the difference is shown between the UAV-derived SMB field and a SMB field
629 only determined by elevation as derived from a linear fit of the stake measurements with altitude. In general, the
630 largest differences occur close to the margin of the glaciers, and around their front. The differences at the glacier
631 margin of Vadret da Morteratsch are mainly related to a thick debris cover, which when sufficient in thickness,
632 has an insulating effect that reduces the glacier melt (e.g. Rounce et al., 2018; Verhaegen et al., 2020). For example,
633 for the heavily-debris covered area where Vadret da Morteratsch protrudes towards the north, the SMB is -1.5 m
634 i.e. yr^{-1} below the debris and up to -12 m i.e. yr^{-1} for the clean ice next to the debris. The melt ratio is therefore
635 equal to 0.125, which means that there is 87.5% less melt under the debris at this location. This corresponds to a
636 debris thickness of more than 50 cm when a typical average value of the characteristic debris thickness is used
637 (Anderson and Anderson, 2016; Rounce et al., 2018). Such thicknesses are very likely in this area where boulders
638 from the lateral moraines supply supraglacial debris.

639

640



641

642

643 **Figure 13.** The inset shows a linear SMB fit based on stake measurements. The main figure shows the difference between the
644 UAV-derived SMB and the linearly derived SMB. The background image is a Sentinel-2 true colour composite satellite image
645 from 13 September 2020. Contour lines are added for every metre. Labels are added for the contour of value 0 m i.e. yr^{-1} .

646



647

648 Another major feature is the presence of patches with a clearly more negative SMB when relying on the UAV-
649 derived SMB field. These differences relate to stationary areas at local ice fronts or collapsing ice caves. While
650 the first are real SMB variations (caused by more irradiation and/or less snow), the latter ones are not caused by
651 the SMB. These collapsing ice caves clearly appear to occur near stagnant ice and at the bottom of the glacier
652 where melt water forms a cave below the ice (Figure 13b). These caves collapse when the overlying ice becomes
653 too thin due to melting at the surface. For the other areas, the difference between the SMB fields is generally
654 smaller, between -0.5 and 0.5 m i.e yr⁻¹. This is in the same order as the MAE and the RMSE and is slightly larger
655 than the expected accuracy of the SMB measurements.

656

657

658 **5 Sensitivity analysis of the selected data, parameters and filters**

659

660 The surface elevation changes and the ice flux divergence contribute separately to the surface mass balance,
661 implying that errors and uncertainties in both terms do not influence each other but directly affect the determined
662 SMB (Eq. 4). It is therefore crucial to determine to which extent the uncertainty of both affects the results of the
663 applied method. In addition, we evaluate the results of the different filter procedures of the ice flux divergence.

664

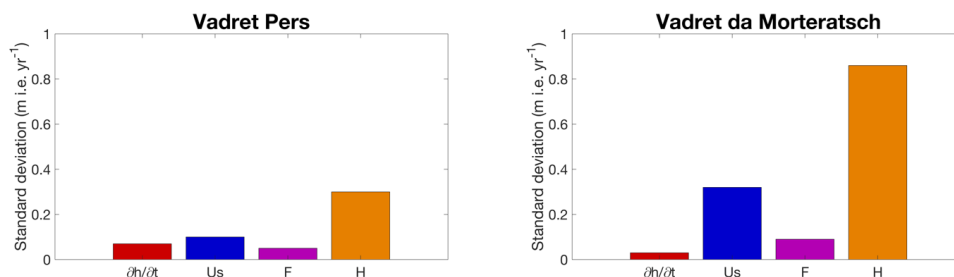
665 **5.1 Dependence on the data and F-value used**

666

667 To study the sensitivity of the applied method to the used data and F-value, we create 100 perturbed fields of the
668 surface elevation changes, the surface velocity, the F-value and the ice thickness. After that, we do the calculations,
669 using the perturbed data for one dataset and the original data for the other ones. Next, the MAE of modelled versus
670 measured SMB is calculated 100 times and the standard deviation of this MAE is determined. The uncertainty in
671 the surface elevation changes is assumed to be correlated in space, i.e. depending on a pattern across the glacier
672 (e.g. Fisher et al., 2015). Therefore, we perturb the $\partial h/\partial t$ fields using randomly spread patches with diameters
673 between 50 m (local errors at grid level) and 500 m with perturbations of maximum 0.5 m (plausible maximum
674 value for UAV data). Regarding surface velocity, we use error estimates of 10% of the observed velocity, similar
675 to the expected accuracy (see section 4.2). Besides velocity itself, the assumption of a constant F-value is rather
676 unrealistic (Zekollari et al., 2013). Ice flow over basal irregularities causes variations in F. Previous research
677 showed for example F to be larger over basal highs and smaller over basal lows and glacier areas with more basal
678 sliding might as well be characterized by a larger F-value (Reeh et al., 2003). Therefore, we apply perturbations
679 using an F-value between 0.85 and 0.95. Concerning ice thickness, we apply perturbations of 30% of the local ice
680 thickness which is mentioned by Zekollari et al. (2013) as an estimate of the accuracy.

681

682



683

684

685 **Figure 14.** Standard deviation of the MAE for the perturbed versions of the surface elevation changes, the surface velocity
686 (u_s), the F-value and the ice thickness (H).

687

688

689 The effect of perturbation of $\partial h/\partial t$ on the determined SMB is small with a standard deviation of less than 0.1 m
690 i.e. yr^{-1} for both glaciers (Figure 14). As a result, the applied method is not very sensitive to (small) perturbations
691 in $\partial h/\partial t$. Changes in the F-value and surface velocity also appear to have minor sensitivity, especially concerning
692 Vadret Pers. Regarding Vadret da Morteratsch, the surface velocity has a SD of 0.3 m i.e. yr^{-1} , which is not
693 negligible (Figure 14). The ice thickness distribution, however, is for both glaciers undoubtedly most crucial for
694 the determination of the SMB, and even more so for Vadret da Morteratsch.

695

696

697 5.2 Evaluation of procedures to filter the ice flux divergence

698

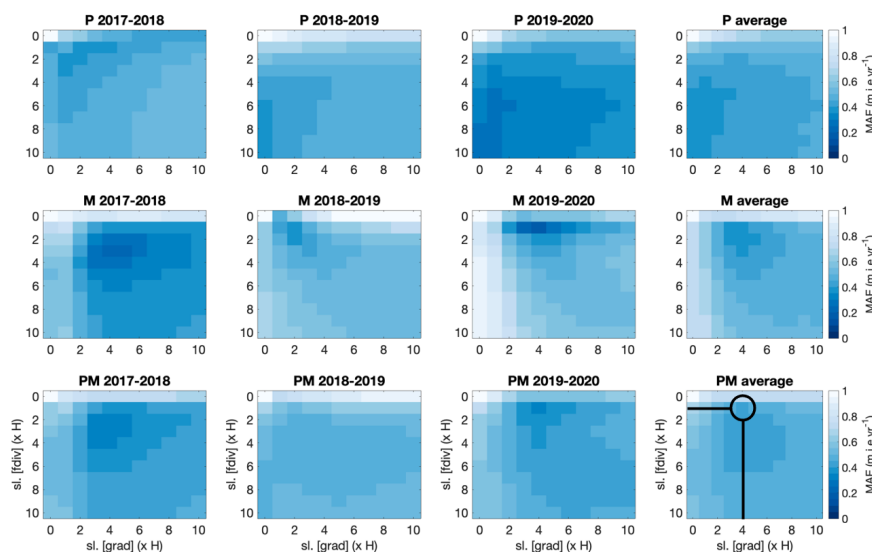
699 As the ice flow at a given location is determined by the surrounding glacier geometry (i.e. not only by its local
700 geometry) and to avoid non-physical oscillations in the flux divergence field (as a result of fine grid spacing), it
701 appears to be necessary to consider various spatial scales over which the ice flux divergence needed to be
702 determined and different filtering procedures (see section 3.4). The results of each possible combination are shown
703 in Figure 15.

704

705 By only applying the exponential decay filter to the ice flux divergence field (moving down in the matrix), we find
706 minimum MAE and RMSE values when the scaling length is equal to seven times H (MAE for Morteratsch-Pers
707 is 0.55 m i.e. yr^{-1}). Such a large scaling length indicates that the ice flux divergence field must be smoothed
708 significantly and therefore becomes entirely smeared with limited variation in the ablation area. One of the reasons
709 for this high value are large ice thickness and velocity gradients resulting from solving ice flow processes on a
710 high-resolution numerical grid. To compensate for the effects of large gradients, the second option is to consider
711 the gradients over larger spatial scales. We do this by applying the exponential filter to the ice thickness and
712 velocity gradients and calculate the ice flux divergence using these smoothed gradients (moving to the right in the
713 matrix). Here, the MAE remains in all experiments above 0.6 m i.e. yr^{-1} . In addition, this value is only reached as
714 soon as the velocity gradient is considered over ten times H and the ice thickness gradients over five times H. The
715 solution to compensate for the negative effects of a very large scaling length for both previous filters and the biases
716 related to both is to filter twice, as was shown in section 4.3. As soon as the ice thickness and velocity gradients



717 and the ice flux divergence are smoothed, the MAE becomes significantly smaller (Figure 15). The MAE is now
718 much below 1 m i.e. yr^{-1} .
719
720



721
722

723 **Figure 15.** Mean absolute error between measured and modelled SMB for various scaling lengths. The scaling length depends
724 on the local ice thickness ($x H$). Smoothing the ice thickness and velocity gradients (grad) or smoothing the ice flux divergence
725 (fdiv) is represented by the horizontal axis and vertical axis, respectively. M represents Vadret da Morteratsch, P represents
726 Vadret Pers and PM represents the entire glacier complex. The plots entitled with average concern the average over all balance
727 years. The selected combination with which the ice flux divergence is calculated as shown in Figure 10 is encircled with black.

728
729
730

Another observation standing out is that concerning Vadret Pers, the MAE mostly decreases when the ice flux
731 divergence is smoothed while for Vadret da Morteratsch, smoothing the gradients has a larger impact (Figure 15).
732 Our explanation for these peculiar differences is that the gradients (both in terms of ice thickness and surface
733 velocity) for Vadret Pers are already significantly smaller compared to those of Vadret da Morteratsch. The latter
734 glacier has both a higher velocity and a larger ice thickness. Consequently, smoothing of the gradients for Vadret
735 da Morteratsch is more decisive, whereas for Vadret Pers it is the other way around.

736
737

738 6 Conclusions

739

740 In this study, a method was presented to estimate the surface mass balance pattern from UAV observations, a
741 known ice thickness field, and the principles of mass continuity. Annual surface elevation changes and surface
742 velocities were quantified from UAV and were shown to have centimetre accuracy. The method was applied to
743 the entire ablation zone of Vadret da Morteratsch and Vadret Pers (Switzerland) for three individual balance years



744 between 2017 and 2020. For the well-studied Morteratsch-Pers glacier complex, we were able to closely reproduce
745 SMB surveyed at about 16 stake locations. A major advantage of using close-range (UAV) remote sensing data is
746 that a significantly more detailed SMB pattern can be obtained over the entire ablation area at a high spatial
747 resolution, which is not feasible with a (small) number of stakes. The need for inter- and extrapolations from a
748 limited number of stakes can introduce several significant errors when the heterogeneity of the glacier surface
749 cannot be captured well from the installed stake positions.

750

751 The analysis did not demonstrate a simple consensus on how to consider the ice flux divergence for optimal results
752 on both glaciers. It proved to be necessary to consider large spatial scales concerning the ice flux divergence to
753 apply the continuity-equation method and closely reproduce the SMB. By using an exponential decay filter to the
754 ice thickness and velocity gradients and the ensuing ice flux divergence over several times the local ice thickness
755 (at least 2x), the mean absolute error between modelled and measured SMB decreased to 0.3-0.7 m i.e. yr⁻¹ on
756 average for the three balance years. Considering the uncertainty of the data and the stake measurements, this is
757 quite accurate.

758

759 The applicability of the applied method to other, less well studied glaciers, depends on how closely the elevation
760 changes, the surface velocities and the ice thickness can be estimated for these ice bodies. In recent years, a new
761 series of methods have arisen from which surface elevation changes and surface velocities can be derived over
762 glaciers (Brun et al., 2017; Paul et al., 2017; Millan et al., 2019; Braun et al., 2019; Nagy et al., 2019; Dussailant
763 et al., 2019; Sommer et al., 2019). This seems encouraging to investigate the applicability using high-resolution
764 satellite data, preferably lower than 10 m for accurate velocity determination. However, our analysis also showed
765 that especially the ice thickness should be well known. The latter seems to hamper the application of the method
766 to many glaciers because large-scale ice thickness estimates are often not accurate enough. As shown in a recent
767 study on four Central Asian glaciers such large-scale thickness estimates may capture the general pattern of the
768 ice thickness distribution and total volume well, but they exhibit significant deviations at the local scale (Van
769 Tricht et al., 2020).

770

771

772

773 **Code and data availability**

774

775 Model code written in Matlab and DSMs will be provided on Github.

776

777

778 **Author contribution**

779

780 LVT developed the method, performed the experiments and wrote the manuscript. PH provided guidance in
781 implementing the research and interpreting the results and assisted during the entire process. JVB and AV
782 contributed to the fieldwork, collaborated in developing the method and improved the manuscript throughout the
783 entire process. KVO assisted during the fieldwork and introduced LVT in using UAVs for research purposes. HZ



784 participated in the fieldwork for many years and contributed throughout the entire process to developing the
785 method and optimising and refining the research.

786

787

788 **Competing interests.**

789

790 The authors declare that they have no conflict of interest.

791

792

793 **Acknowledgements**

794

795 The authors would like to thank Chloe Marie Paice, Felix Vanderleenen, He Zhang, Robbe Neyns, Steven De
796 Hertog, Veronica Tollenaar and Yoni Verhaegen, who assisted during the fieldwork to perform stake
797 measurements and distribute and collect GCPs.

798

799

800 **Financial Support**

801

802 Lander Van Tricht holds a PhD fellowship of the Research Foundation-Flanders (FWO-Vlaanderen) and is
803 affiliated with the Vrije Universiteit Brussel (VUB). Harry Zekollari contributed to the fieldwork as a PhD fellow
804 of the Research Foundation-Flanders (FWO-Vlaanderen) and at a later stage as a Marie Skłodowska-Curie fellow
805 at the TU Delft (grant 799904). K Van Oost is an FNRS Research Director.

806

807

808



809 **7 References**

810

811 Anderson, L. S. and Anderson, R. S.: Modeling debris-covered glaciers: response to steady
812 debris deposition, *The Cryosphere*, 10, 1105–1124, <https://doi.org/10.5194/tc-10-1105-2016>, 2016

813

814 Berthier, E. and Vincent, C.: Relative contribution of surface mass-balance and ice-flux changes to the
815 accelerated thinning of Mer de Glace, French Alps, over 1979–2008, *Journal of Glaciology*, 58(209),
816 501–512, <https://doi.org/10.3189/2012JoG11J083>, 2012

817

818 Bisset, R. R., Dehecq, A., Goldberg, D. N., Huss, M., Bingham, R. G., and Gourmelen, N.: Reversed Surface-
819 Mass-Balance Gradients on Himalayan Debris-Covered Glaciers Inferred from Remote Sensing, 12,
820 <https://doi.org/10.3390/rs12101563>, 2020.

821

822 Braithwaite, R. J.: Glacier mass balance: the first 50 years of international monitoring, *Progress in Physical*
823 *Geography*, 26,76–95, <https://doi.org/10.1191/0309133302pp326ra>, 2002

824

825 Braun, M.H., Malz, P., Sommer, C., Fariás-Barahona, D., Sauter, T., Casassa, G., Soruco, A., Skvarca, P. and
826 Seehaus, T.C.: Constraining glacier elevation and mass changes in South America, *Nature Climate*
827 *Change*, 9(2), 130–136, <https://doi.org/10.1038/s41558-018-0375-7>, 2019

828

829 Brun, F., Berthier, E., Wagnon, P., Kääb, A. and Treichler, D.: A spatially resolved estimate of High Mountain
830 Asia glacier mass balances from 2000 to 2016, *Nature Geoscience*, 10, 668–673,
831 <https://doi.org/10.1038/ngeo2999>, 2017

832

833 Davaze, L., Rabatel, A., Dufour, A., Hugonnet, R. and Arnaud, Y.: Region-Wide Annual Glacier Surface
834 Mass Balance for the European Alps From 2000 to 2016, *Frontiers in Earth Science*, 8, 0–14,
835 <https://doi.org/10.3389/feart.2020.00149>, 2020

836

837 Dehecq, A., Gourmelen, N., Gardner, A.S., Brun, F., Goldberg, D., Nienow, P.W., Berthier, E., Vincent, C.,
838 Wagnon, P. and Trouvé, E.: Twenty-first century glacier slowdown driven by mass loss in High
839 Mountain Asia, *Nature Geoscience*, 12, 22–27, <https://doi.org/10.1038/s41561-018-0271-9>, 2019

840

841 Dussailant, I., Berthier, E., Brun, F., Masiokas, M., Hugonnet, R., Favier, V., Rabatel, A., Pitte, P. and Ruiz, L.:
842 Two decades of glacier mass loss along the Andes, *Nature Geoscience*, 12, 802–808,
843 <https://doi.org/10.1038/s41561-019-0432-5>, 2019

844

845 Fischer, M., Huss, M. and Hoelzle, M.: Surface elevation and mass changes of all Swiss glaciers 1980–
846 2010, *The Cryosphere*, 9, 525–540, <http://doi.org/10.5194/tc-9-525-2015>, 2015

847

848 Gindraux, S., Boesch, R. and Farinotti, D.: Accuracy Assessment of Digital Surface Models from



- 849 Unmanned Aerial Vehicles' Imagery on Glaciers, *Remote Sensing*, 9(2),
850 186, <https://doi.org/10.3390/rs9020186>, 2017
851
- 852 Goldstein, E.B., Oliver, A.R., deVries, E., Moore, L.J. and Jass, T.: Ground control point requirements for
853 structure-from-motion derived topography in low-slope coastal environments, *PeerJPrePrints*
854 3:e1444v1, <https://doi.org/10.7287/peerj.preprints.1444v1>, 2015
855
- 856 Gudmundsson, G.H. and Bauder, A.: Towards an Indirect Determination of the Mass-balance Distribution of
857 Glaciers using the Kinematic Boundary Condition, *Geografiska Annaler*, 81(4), 575–583,
858 <https://doi.org/10.1111/1468-0459.00085>, 1999
859
- 860 Heid, T., and Käab, A.: Evaluation of existing image matching methods for deriving glacier surface
861 displacements globally from optical satellite imagery, *Remote Sensing of Environment*, 118, 339–355,
862 <https://doi.org/10.1016/j.rse.2011.11.024>, 2012
863
- 864 Hubbard, A., Willis, I., Sharp, M., Mair, D., Nienow, P., Hubbard, B. and Blatter, H.: Glacier mass-balance
865 determination by remote sensing and high-resolution modelling, *Journal of Glaciology*, 46(154), 491–
866 498, <https://doi.org/10.3189/172756500781833016>, 2000
867
- 868 Huss, M., Dhulst, L., and Bauder, A.: New long-term mass-balance series for the Swiss Alps, *Journal of*
869 *Glaciology*, 61(227), 551-562, <https://doi.org/10.3189/2015JoG15J015>, 2015
870
- 871 Hutter, R.K. and Morland, L.W.: Euromech colloquium 172: Mechanics of glaciers, Interlaken, 19–23
872 September, 1983, *Cold Regions Science and Technology*, 9(1), 77-86, [https://doi.org/10.1016/0165-](https://doi.org/10.1016/0165-232X(84)90049-1)
873 [232X\(84\)90049-1](https://doi.org/10.1016/0165-232X(84)90049-1), 1984
874
- 875 Immerzeel, W.W., Kraaijenbrink, P.D.A., Shea, J.M., Shrestha, A.B., Pellicciotti, F., Bierkens, M.F.P. and de
876 Jong, S.M.: High-resolution monitoring of Himalayan glacier dynamics using unmanned aerial vehicles,
877 *Remote Sensing of Environment*, 150, 93–103, <https://doi.org/10.1016/j.rse.2014.04.025>, 2014
878
- 879 Käab, A. and Funk, M.: Modelling mass balance using photogrammetric and geophysical data: a pilot
880 Study at Griesgletscher, Swiss Alps, *Journal of Glaciology*, 45(151), 575–583,
881 <https://doi.org/10.3189/S0022143000001453>, 1999
882
- 883 Kamb, B. and Echelmeyer, K.A.: Stress-gradient Coupling in Glacier Flow: IV. Effects of the “ T ”
884 Term, *Journal of Glaciology*, 32(112), 342–349, <https://doi.org/10.3189/S0022143000012016>, 1986
885
- 886 Kaser, G., Fountain, A., and Jansson, P.: A manual for monitoring the mass balance of mountain glaciers,
887 *International Hydrological Programme (IHP-VI. Technical Documents in Hydrology 59)*, UNESCO,
888 Paris, 2003.



- 889
890
891 Kienholz, C., Pierce, J., Hood, E., Amundson, J.M., Wolken, G.J., Jacobs, A., Hart, S., Wikstrom, Jones K.,
892 Abdel-Fattah, D., Johnson, C. and Conaway, J.S.: Deglaciation of a Marginal Basin and
893 Implications for Outburst Floods, Mendenhall Glacier, Alaska. *Frontiers in Earth Science*, 8, 1–21
894 <https://doi.org/10.3389/feart.2020.00137>, 2020
895
896 Langhammer, L., Grab, M., Bauder, A. and Maurer, H.: Glacier thickness estimations of alpine glaciers
897 using data and modeling constraints, *The Cryosphere*, 13(8), 2189–2202, [https://doi.org/10.5194/tc-13-](https://doi.org/10.5194/tc-13-2189-2019)
898 [2189-2019](https://doi.org/10.5194/tc-13-2189-2019), 2019
899
900 Le Brocq, A.M., Payne, A.J. and Siegert, M.J.: West Antarctic balance calculations: Impact of flux-routing
901 algorithm, smoothing algorithm and topography. *Computers and Geosciences*, 32(10), 1780–1795,
902 <https://doi.org/10.1016/j.cageo.2006.05.003>, 2006
903
904 Long, N., Millescamps, B., Pouget, F., Dumon, A., Lachaussée, N. and Bertin, X.: Accuracy assessment of
905 coastal topography derived from UAV images, *The International Archives of the Photogrammetry,*
906 *Remote Sensing and Spatial Information Sciences*, XLI-B1, 1127–1134, [https://doi.org/10.5194/isprs-](https://doi.org/10.5194/isprs-archives-XLI-B1-1127-2016)
907 [archives-XLI-B1-1127-2016](https://doi.org/10.5194/isprs-archives-XLI-B1-1127-2016), 2016
908
909 Marzeion, B., Hock, R., Anderson, B., Bliss, A., Champollion, N., Fujita, K., Huss, M., Immerzeel, W.W.,
910 Kraaijenbrink, P., Malles, J., Maussion, F., Radić, V., Rounce, D.R., Sakai, A., Shannon, S., Wal, R.
911 and Zekollari, H.: Partitioning the Uncertainty of Ensemble Projections of Global Glacier Mass Change,
912 *Earth's Future*, 8(7), 1–25, <https://doi.org/10.1029/2019EF001470>, 2020
913
914 Messerli, A. and Grinsted, A.: Image georectification and feature tracking toolbox: ImGRAFT, *Geoscientific*
915 *Instrumentation Methods and Data Systems*, 4, 23–34, <https://doi.org/10.5194/gi-4-23-2015>, 2015
916
917 Millan, R., Mouginot, J., Rabatel, A., Jeong, S., Cusicanqui, D., Derkacheva, A., and Chekki, M.: Mapping
918 Surface Flow Velocity of Glaciers at Regional Scale Using a Multiple Sensors Approach, 11,
919 <https://doi.org/10.3390/rs11212498>, 2019
920
921 Nagy, T., Andreassen, L.M., Duller, R.A. and Gonzalez, P.J.: SenDiT: The Sentinel-2 Displacement Toolbox
922 with Application to Glacier Surface Velocities. *Remote Sensing*, 11(10), 1151,
923 <https://doi.org/10.3390/rs11101151>, 2019
924
925 Nemeč, J., Huybrechts, P., Rybak, O. and Oerlemans, J.: Reconstruction of the annual balance of
926 Vadret da Morteratsch, Switzerland, since 1865, *Annals of Glaciology*, 50(50), 126–134,
927 <https://doi.org/10.3189/172756409787769609>, 2009
928



- 929 Nuimura, T., Fujita, K., Fukui, K., Asahi, K., Aryal, R. and Ageta, Y.: Temporal Changes in Elevation of the
930 Debris-Covered Ablation Area of Khumbu Glacier in the Nepal Himalaya since 1978, *Arctic Antarctic*
931 *Alpine Research*, 43(2), 246–255, <https://doi.org/10.1657/1938-4246-43.2.246>, 2011
932
- 933 Paul, F., Bolch, T., Briggs, K., Kääb, A., McMillan, M., McNabb, R., Nagler, T., Nuth, C., Rastner, P., Strozzi,
934 T. and Wuite, J.: Error sources and guidelines for quality assessment of glacier area, elevation change,
935 and velocity products derived from satellite data in the *Glaciers_cci* project. *Remote Sensing of*
936 *Environment*, 203, 256–275, <https://doi.org/10.1016/j.rse.2017.08.038>, 2017
937
- 938 Reeh, N., Mohr, J.J., Krabill, W.B., Thomas, R., Oerter, H., Gundestrup, N. and Bøggild, C.E.: Glacier specific
939 ablation rate derived by remote sensing measurements. *Geophysical Research Letters*, 29(16), 10-1-10–
940 4, <https://doi.org/10.1029/2002GL015307>, 2002
941
- 942 Reeh, N., Mohr, J.J., Madsen, S.N., Oerter, H. and Gundestrup, N.S.: Three-dimensional surface velocities
943 of Storstrømmen glacier, Greenland, derived from radar interferometry and ice-sounding radar
944 measurements, *Journal of Glaciology*, 49(165), 201–209,
945 <https://doi.org/10.3189/172756503781830818>, 2003
946
- 947 Reznichenko, N., Davies, T., Schulmeister, J. and McSaveney, M.: Effects of debris on ice-surface melting
948 rates: an experimental study, *Journal of Glaciology*, 56(197), 384–394,
949 <https://doi.org/10.3189/002214310792447725>, 2010
950
- 951 Rounce, D.R., King, O., McCarthy, M., Shean, D.E. and Salerno, F.: Quantifying Debris Thickness of Debris-
952 Covered Glaciers in the Everest Region of Nepal Through Inversion of a Subdebris Melt Model. *Journal*
953 *of Geophysical Research Earth Surface*, 123(5), 1094–1115, <https://doi.org/10.1029/2017JF004395>,
954 2018
955
- 956 Ruiz, L., Berthier, E., Masiokas, M., Pitte, P. and Villalba, R.: First surface velocity maps for glaciers of
957 Monte Tronador, North Patagonian Andes, derived from sequential Pléiades satellite images, *Journal of*
958 *Glaciology*, 61(229), 908–922, <https://doi.org/10.3189/2015JoG14J134>, 2015
959
- 960 Ryan, J.C., Hubbard, A.L., Box, J.E., Todd, J., Christoffersen, P., Carr, J.R., Holt, T.O. and Snooke N.: UAV
961 photogrammetry and structure from motion to assess calving dynamics at Store Glacier, a large outlet
962 draining the Greenland ice sheet, *The Cryosphere*, 9(1), 1–11, <https://doi.org/10.5194/tc-9-1-2015>, 2015
963
- 964 Seroussi, H., Morlighem, M., Rignot, E., Larour, E., Aubry, D., Ben Dhia, H. and Kristensen, S.S.: Ice flux
965 divergence anomalies on 79north Glacier, Greenland, *Geophysical Research Letters*, 38(9), L09501,
966 <https://doi.org/10.1029/2011GL047338>, 2011
967
- 968 Sommer, C., Malz, P., Seehaus, T.C., Lippl, S., Zemp, M. and Braun, M.H.: Rapid glacier retreat and



- 969 downwasting throughout the European Alps in the early 21st century, *Nature Communications*, 11(1),
970 3209, <https://doi.org/10.1038/s41467-020-16818-0>, 2020
971
- 972 Tahar, K.N., Ahmad, A., Aziz, W.A., Akib, W.M., Mohd, W. and Mohd, N.W.: Assessment on Ground Control
973 Points in Unmanned Aerial System Image Processing for Slope Mapping Studies. *International Journal*
974 *of Scientific & Engineering Research*, 3(11), 1-10, 2012
975
- 976 Tonkin, T. and Midgley, N.: Ground-Control Networks for Image Based Surface Reconstruction: An
977 Investigation of Optimum Survey Designs Using UAV Derived Imagery and Structure-from-Motion
978 Photogrammetry, *Remote Sensing*, 8(9), 786, <https://doi.org/10.3390/rs8090786>, 2016
979
- 980 Van Tricht, L., Huybrechts, P., Van Breedam, J., Fürst, J.J., Rybak, O., Satylkanov, R., Ermenbaiev, B., Popovnin,
981 V., Neyns, R., Paice, C.M. and Malz, P.: Measuring and inferring the ice thickness distribution of four
982 glaciers in the Tien Shan, Kyrgyzstan, *Journal of Glaciology*, 1–18, <https://doi.org/10.1017/jog.2020.104>,
983 2020
984
- 985 Verhaegen, Y., Huybrechts, P., Rybak, O., and Popovnin, V. V.: Modelling the evolution of Djankuat Glacier,
986 North Caucasus, from 1752 until 2100 CE, *The Cryosphere*, 14, 4039–4061, [https://doi.org/10.5194/tc-](https://doi.org/10.5194/tc-14-4039-2020)
987 [14-4039-2020](https://doi.org/10.5194/tc-14-4039-2020), 2020.
988
- 989 Vincent, C., Wagon, P., Shea, J. M., Immerzeel, W. W., Kraaijenbrink, P., Shrestha, D., Soruco, A., Arnaud,
990 Y., Brun, F., Berthier, E., and Sherpa, S. F.: Reduced melt on debris-covered glaciers: investigations
991 from Changri Nup Glacier, Nepal, *The Cryosphere*, 10, 1845–1858, [https://doi.org/10.5194/tc-](https://doi.org/10.5194/tc-10-1845-2016)
992 [10-1845-](https://doi.org/10.5194/tc-10-1845-2016)
993 [2016](https://doi.org/10.5194/tc-10-1845-2016), 2016.
- 994 Vincent, C., Cusicanqui, D., Jourdain, B., Laarman, O., Six, D., Gilbert, A., Walpersdorf, A., Rabatel, A., Piard,
995 L., Gimbert, F., Gagliardini, O., Peyaud, V., Arnaud, L., Thibert, E., Brun, F., and Nanni, U.: Geodetic
996 point surface mass balances: A new approach to determine point surface mass balances from remote
997 sensing measurements, *The Cryosphere Discuss.* [preprint], [https://doi.org/10.5194/tc-](https://doi.org/10.5194/tc-2020-239)
998 [2020-239](https://doi.org/10.5194/tc-2020-239), in
999 review, 2020.
- 1000 Whitehead, K., Moorman, B. J., and Hugenholtz, C. H.: Brief Communication: Low-cost, on-demand aerial
1001 photogrammetry for glaciological measurement, *The Cryosphere*, 7, 1879–1884,
1002 <https://doi.org/10.5194/tc-7-1879-2013>, 2013.
1003
- 1004 Wigmore, O. and Mark, B.: Monitoring tropical debris-covered glacier dynamics from high-resolution
1005 unmanned aerial vehicle photogrammetry, Cordillera Blanca, Peru, *The Cryosphere*, 11, 2463–2480,
1006 <https://doi.org/10.5194/tc-11-2463-2017>, 2017.
1007
- 1008 Wouters, B., Gardner, A.S. and Moholdt, G.: Global Glacier Mass Loss During the GRACE Satellite



- 1009 Mission (2002-2016), *Frontiers in Earth Science*, 7, 1–11, <https://doi.org/10.3389/feart.2019.00096>,
1010 2019
1011
- 1012 Yang, W., Zhao, C., Westoby, M., Yao, T., Wang, Y., Pellicciotti, F., Zhou, J., He, Z. and Miles, E.: Seasonal
1013 Dynamics of a Temperate Tibetan Glacier Revealed by High-Resolution UAV Photogrammetry and In
1014 Situ Measurements, *Remote Sensing*, 12(15), 2389, <https://doi.org/10.3390/rs12152389>, 2020
1015
- 1016 Zekollari, H., Huybrechts, P., Fürst, J.J., Rybak, O. and Eisen, O.: Calibration of a higher-order 3-D ice-
1017 flow model of the Morteratsch glacier complex, Engadin, Switzerland, *Annals of Glaciology*, 54(63),
1018 343–351, <https://doi.org/10.3189/2013AoG63A434>, 2013
1019
- 1020 Zekollari, H., Fürst, J.J. and Huybrechts, P.: Modelling the evolution of Vadret da Morteratsch,
1021 Switzerland, since the Little Ice Age and into the future, *Journal of Glaciology*, 60(224), 1155–1168,
1022 <https://doi.org/10.3189/2014JoG14J053>, 2014
1023
- 1024 Zekollari, H. and Huybrechts, P.: On the climate–geometry imbalance, response time and volume–area
1025 scaling of an alpine glacier: insights from a 3-D flow model applied to Vadret da Morteratsch,
1026 Switzerland, *Annals of Glaciology*, 56(70), 51–62, <https://doi.org/10.3189/2015AoG70A921>, 2015
1027
- 1028 Zekollari, H. and Huybrechts, P.: Statistical modelling of the surface mass-balance variability of the
1029 Morteratsch glacier, Switzerland: strong control of early melting season meteorological conditions,
1030 *Journal of Glaciology*, 64(244), 275–288, <https://doi.org/10.1017/jog.2018.18>, 2018
1031
- 1032
- 1033 Zekollari, H., Huss, M., and Farinotti, D.: Modelling the future evolution of glaciers in the European Alps under
1034 the EURO-CORDEX RCM ensemble, *The Cryosphere*, 13, 1125–1146, <https://doi.org/10.5194/tc-13-1125-2019>, 2019.
1035
- 1036
- 1037 Zemp, M., Thibert, E., Huss, M., Stumm, D., Denby, C.R., Nuth, C., Nussbaumer, S.U., Moholdt, G., Mercer,
1038 A., Mayer, C., Joerg, P.C., Jansson, P., Hynek, B., Fischer, A., Escher-Vetter, H., Elvehøy, H. and
1039 Andreassen, L.M.: Uncertainties and re-analysis of glacier mass balance measurements Uncertainties
1040 and re-analysis of glacier mass balance measurements, *The Cryosphere Discussions*, 7(2), 789–839,
1041 <https://doi.org/10.5194/tcd-7-789-2013>, 2013
1042
- 1043 Zemp, M., Huss, M., Thibert, E., Eckert, N., McNabb, R., Huber, J., Barandun, M., Machguth, H., Nussbaumer,
1044 S.U., Gärtner-Roer, I., Thomson, L., Paul, F., Maussion, F., Kutuzov, S. and Cogley, J.G.: Global
1045 glacier mass changes and their contributions to sea-level rise from 1961 to 2016, *Nature*, 568, 382–386,
1046 <https://doi.org/10.1038/s41586-019-1071-0>, 2019
1047
- 1048 Zhang, H., Aldana-Jague, E., Clapuyt, F., Wilken, F., Vanacker, V., and Van Oost, K.: Evaluating the potential



1049 of post-processing kinematic (PPK) georeferencing for UAV-based structure- from-motion (SfM)
1050 photogrammetry and surface change detection, Earth Surf. Dynam., 7, 807–827,
1051 <https://doi.org/10.5194/esurf-7-807-2019>, 2019.
1052
1053